Melatonin Enhances Sleep via MT_1-Driven Activation of Slo1 in Suprachiasmatic Nucleus Neurons

Kiranmayi Vedantham[1#], Adeel Ahmad[1#], Longgang Niu[1#], Yuan Shui[1], Fouad Lemtiri-Chlieh[1], Deborah Kaback[2], Xin-Ming Ma[1], Siu-Pok Yee[2], and Zhao-Wen Wang[1*]

Institutional Affiliations

[1]Department of Neuroscience and [2]Center of Mouse Genome Modification, University of Connecticut School of Medicine, Farmington, CT, USA

[#]Equal contributions.

***Correspondence**

Zhao-Wen Wang

Email: zwwang@uchc.edu

SUMMARY

Melatonin is known to promote sleep, but its underlying molecular mechanisms remain poorly understood. Using CBA/CaJ mice, a strain capable of melatonin synthesis, we explored the roles of the BK channel (Slo1) and the melatonin receptor MT_1 in regulating sleep behavior and action potentials in the suprachiasmatic nucleus (SCN). Global knockout of Slo1 or MT_1 reduced REM and NREM sleep, increased wakefulness, and broadened action potentials while abolishing afterhyperpolarization in SCN neurons. These effects were primarily or exclusively observed during the subjective daytime, when mice are less active. Consistent with this, Slo1 expression in the SCN was markedly higher during the day than at night. Slo1 knockout mice also exhibited pronounced seizure activity. Through deletion analyses, we identified key domains in MT_1 and Slo1 that are essential for their physical interaction. Together, these findings suggest that melatonin promotes sleep by activating Slo1 in the SCN through an MT_1-mediated signaling pathway.

INTRODUCTION

Melatonin, often referred to as the "dark hormone" or "sleep hormone", is a key regulator of circadian rhythms and sleep. It acts through two G protein-coupled receptors: MT_1 and MT_2 [1]. While melatonin is thought to promote sleep by reducing cytosolic cAMP levels via the $G\alpha_i$ signaling pathway of G_i-type G proteins [1], the downstream molecular target(s) mediating this effect remains elusive.

The suprachiasmatic nucleus (SCN) of the hypothalamus serves as the master circadian clock, synchronizing physiological and behavioral rhythms—such as sleep-wake cycles, melatonin secretion, and body temperature—to the light-dark cycle via photic input from the retina [2-5]. Within the SCN, numerous proteins contribute to these regulatory functions, including ion channels that modulate neuronal excitability and firing patterns [6].

Slo1 (also known as the BK channel), a large-conductance potassium channel activated by membrane depolarization and cytosolic calcium [7], is prominently expressed in the SCN. Its expression and activity exhibit a circadian rhythm, with higher protein levels and larger currents during the subjective night compared to the day [8-10]. Genetic ablation of *Kcnma1*, the gene encoding the pore-forming subunit of Slo1, increases SCN neuronal firing rate at night [8], while knockout of *Kcnmb2*, which encodes the β2-subunit that facilitates channel inactivation, disrupts the daily rhythm in SCN firing rates[9]. Additionally, knockout of either *Kcnma1* or *Kcnmb2* alters circadian rhythms in locomotor activity [8,9]. These findings suggest that Slo1 plays an important role in regulating SCN neuronal activity, particularly during the night when mice are active. However, whether Slo1 contributes to sleep behavior remains unclear.

MT_1 melatonin receptors are also expressed in the SCN [11-14], but a potential interaction between MT_1 and Slo1 in this region has not been explored. Our recent work in *C. elegans* revealed that melatonin promotes sleep by activating SLO-1, the orthologue of mammalian Slo1, in neurons [15]. Furthermore, we demonstrated that melatonin can activate human Slo1 through MT_1, but not MT_2, in a heterologous expression system, and that this activation is mediated by Gβγ rather than the $G\alpha_i$ pathway [15]. However, it remains unknown whether melatonin can activate Slo1 in mammalian neurons or whether such an interaction regulates neuronal function and sleep behavior.

Loss-of-function mutations in *Slo1* are frequently associated with seizures in humans [16-18]. However, studies in *Kcnma1* knockout mice have yielded conflicting results. While one study reported spontaneous seizure-like behavior [18], another found no evidence of spontaneous seizures or differences in pentylenetetrazol-induced seizure susceptibility [19]. These discrepancies raise questions about the suitability of mouse models for studying Slo1 deficiency-associated seizures and underscore the need for further investigation.

In this study, we investigated whether MT_1 and Slo1 regulate the electrical properties of SCN neurons and sleep behavior in mice. We generated knockout strains for *Mtnr1a* (encoding MT_1) and *Kcnma1* in the CBA/CaJ genetic background, a strain that produces melatonin due to intact melatonin synthesis pathways [20-22]. Using whole-cell patch-clamp recordings in SCN brain slices, we examined neuronal electrical properties, while electroencephalogram (EEG) and electromyogram (EMG) recordings were used to monitor sleep and locomotor behavior. Additionally, we explored whether MT_1 and Slo1 physically interact and which specific domains mediate these interactions using coimmunoprecipitation assays.

Our results demonstrate that knockout of either *Kcnma1* or *Mtnr1a* prolongs action potential (AP) duration in SCN neurons and shortens both REM and NREM sleep durations, primarily during the subjective day. Surprisingly, Slo1 expression in the SCN was higher during the subjective day, contrasting

with previous reports of nighttime-specific effects. We also found that MT_1 and Slo1 physically interact, with the membrane spanning region of MT_1 and the S0-S1 intracellular loop of Slo1 playing key roles. Notably, *Kcnma1*$^{-/-}$ mice exhibited seizure activity, while *MT*$_1^{-/-}$ mice did not. These findings suggest that melatonin promotes sleep by activating Slo1 in the SCN via MT_1, providing new insights into the circadian control of sleep.

RESULTS

Generation of *MT*$_1$ and *Slo1* knockout mice

We used the CRISPR-Cas9 system to generate knockout strains for *Mtnr1a* and *Kcnma1*, referred to as *MT*$_1^{-/-}$ and *Slo1*$^{-/-}$, respectively. Littermate controls are designated as *MT*$_1^{+/+}$ and *Slo1*$^{+/+}$.

The *MT*$_1^{-/-}$ strain carries a 500 bp deletion that eliminates the entire first exon, along with adjacent promoter and intronic regions (**Figure 1A-C and Figure S1A, B**). The removal of exon 1's coding sequence and the splice donor site for exon 2 (the gene has only two exons) renders this mutation null, preventing the production of any MT_1 protein.

The *Slo1*$^{-/-}$ strain has an 866 bp deletion (with a 3 bp insertion) that removes the entire exon 8 (as designated in *Kcnma1* isoform 203), along with portions of the adjacent introns 7 and 8 (**Figure 1D-F and Figure S1C, D**). Exon 8 is conserved across all *Kcnma1* isoforms and encodes a critical region of the Slo1 channel, including 4 residues in the S5 transmembrane segment, the channel pore, and 16 residues in the S6 transmembrane segment (**Figure 1D**). This in-frame deletion abolishes potassium conductance but may still allow the production of a defective Slo1 protein.

Knockout of Slo1 or *MT*$_1$ reduces sleep duration

We investigated the effects of *MT*$_1^{-/-}$ and *Slo1*$^{-/-}$ on sleep-wake behavior by performing EEG and EMG recordings on mice under regular light/dark cycle (12:12). Periods of wakefulness, NREM sleep, and REM sleep were identified by analyzing corresponding EEG and EMG traces. Wakefulness period was characterized by low-amplitude EEG and high-amplitude EMG; NREM period by high-amplitude EEG with a dominant frequency of < 4 Hz and low-amplitude EMG; and REM period by low- or high-amplitude EEG with a dominant frequency between 4 and 8 Hz and low-amplitude EMG (**Figure 2A**).

During the subjective day (light on), both *MT*$_1^{-/-}$ and *Slo1*$^{-/-}$ mice exhibited significantly increased wake time and decreased NREM and REM durations, with an apparently greater reduction in REM than NREM (**Figure 2B, C**). The magnitudes of changes in wake time, NREM duration, and REM duration caused by *MT*$_1^{-/-}$ and *Slo1*$^{-/-}$ compared to littermate controls averaged 18.8% and 39.2%, 9.5% and 20.1%, and 59.6% and 73.5%, respectively. During the subjective night (light off), *MT*$_1^{-/-}$ mice showed no significant differences compared to littermate controls, whereas *Slo1*$^{-/-}$ mice displayed significant decreases in both NREM and REM sleep durations and a significant increase in wake time (**Figure 2B, D**). The distribution patterns of male and female data points in the bar graphs (**Figure 2C, D**) suggest that *MT*$_1^{-/-}$ and *Slo1*$^{-/-}$ exert similar effects on sleep behavior in male and female mice.

Knockout of Slo1, but not MT$_1$, causes significant ictal EEG activity

Our analysis of EEG data revealed frequent high-amplitude, rhythmic electrical discharges in *Slo1*$^{-/-}$ mice, characteristic of seizure activity (**Figure 3A**). These discharges occurred almost exclusively between Zeitgeber time (ZT) 5 and ZT 21 and were not observed in *MT*$_1^{-/-}$ mice or littermate controls.

We quantified the number of ictal events, the total power of each event, and the cumulative power of all ictal events in each mouse. The mean ictal event number between ZT 5 and ZT 21 in *Slo1*$^{-/-}$ mice was 17.5 ± 1.8, with a mean duration of 17.6 ± 1.4 seconds.

To compare power levels, we randomly selected 18 EEG segments from each *Slo1*$^{+/+}$ mouse, with each being 17.6 seconds long to match the number and duration of ictal events in *Slo1*$^{-/-}$ mice. The cumulative power in these segments from wild-type mice was then compared to that of *Slo1*$^{-/-}$ mice, revealing a more than 40-fold increase in cumulative power in *Slo1*$^{-/-}$ mice (**Figure 3B**).

Additionally, we divided the cumulative power into four equal time periods (4 hours each) and compared them to those of *Slo1*$^{+/+}$ mice. This analysis showed that ictal activity in Slo1-/- mice increased gradually over successive periods (**Figure 3C**).

Together, our analysis indicates that *Slo1*$^{-/-}$ leads to strong seizure activity occurring within a specific time window of the day. Since we quantified seizure activity only for ictal events lasting ≥10 seconds, the actual magnitude of the difference between *Slo1*$^{+/+}$ and *Slo1*$^{-/-}$ mice is larger than shown in the figure.

Notably, the periods of high seizure activity (occurring between ZT 5 and ZT 21, with gradually increasing activity over this period) largely overlapped with the time window when *Slo1*$^{-/-}$ mice, but not *MT*$_1^{-/-}$ mice, exhibited decreased REM and NREM sleep and increased wakefulness. This temporal correlation suggests the increased seizure activity in *Slo1*$^{-/-}$ mice contributed to the observed alterations in sleep and wake behaviors.

***Knockout of Slo1* or *MT*$_1$ broadens APs and suppresses AHP in SCN neurons during the daytime**

Where might MT_1 and Slo1 function to regulate sleep? To address this question, we analyzed the effects of *Slo1*$^{-/-}$ and *MT*$_1^{-/-}$ on SCN neuronal electrical properties. Given that both *Slo1*$^{-/-}$ and *MT*$_1^{-/-}$ exhibited differing effects on sleep between the daytime and nighttime, we investigated their effects on SCN neurons in both the subjective day and night. Daytime effects were assessed using mice housed under a light cycle with lights on from 7:00 am to 7:00 pm and off from 7:00 pm to 7:00 am. Brain slices were prepared between 10:00 and 11:00 am and used for electrophysiological experiments between 2:00 and 5:00 pm, corresponding to ZT 3-4 and ZT 7–10, respectively.

We performed whole-cell patch-clamp experiments on neurons located in the ventromedial SCN. Our daytime experiments utilized strains of *Slo1*$^{-/-}$ and *MT*$_1^{-/-}$ single knockout, their littermate controls, as well as *Slo1*$^{-/-}$ and *MT*$_1^{-/-}$ double knockout.

There were no significant differences in membrane resistance (R_m) or resting membrane potential (RPM) between the different groups (**Figure 4A**). AP frequencies in response to current injections (-10 pA to 20 pA in 5-pA increments, with a pulse duration of 5 seconds) tended to increase with higher current injections; however, there was no significant difference between the different groups at each current injection step (**Figure 4B**), suggesting that neither Slo1 nor MT_1 significantly influence AP frequency.

We selected APs induced by current injections of 15 pA and 20 pA for quantitative analysis and quantified several AP-related parameters, including AP duration at 50% repolarization (APD_{50}), maximum and minimum slopes, threshold, amplitude, and afterhyperpolarization (AHP) using the Igor Pro 9 software (Sutter Instrument, Novato, CA) (**Figure 4C-K and Figure S2A-H**). Both *Slo1*$^{-/-}$ and *MT*$_1^{-/-}$ mice showed a substantial increase in APD_{50}, and this phenotype was not aggravated in *Slo1* and *MT*$_1$ double knockout mice (**Figure 4E, F; Figure S2B, C**). The prolongation of APD50 was mainly due to differences between the knockout mice and littermate controls in the rate of AP repolarization rather that of AP rise, as indicated by AP waveform differences between wild-type and knockout mice (**Figure 4E**; **Figure S2B**) and the

comparisons of the maximum and minimum slopes (**Figure 4G, H; Figure S2D, E**). While $MT_1^{-/-}$ mice showed no difference in action potential (AP) threshold and AP amplitude compared to littermate controls, $Slo1^{-/-}$ mice had significantly lower AP thresholds and reduced AP amplitudes; however, the reduction in AP amplitude was only statistically significant when APs were induced by 20-pA current injections, not by 15-pA injections (**Figure 4I, J; Figure S2F, G**). These results indicate that both Slo1 and MT_1 are crucial for AP repolarization, and a loss of their function significantly prolongs AP duration.

Knockout mice also exhibited a markedly suppressed AHP, defined as the hyperpolarized membrane voltage level (relative to the threshold) following each AP in $Slo1^{+/+}$ and $MT_1^{+/+}$ mice. While AHP was obvious in the littermate controls, it was absent in $Slo1^{-/-}$ and $MT_1^{-/-}$ mice (**Figure 4E; Figure S2B**). To quantitatively illustrate this difference, we quantified AHP in $Slo1^{+/+}$ and $MT_1^{+/+}$ mice automatically using the Igor Pro 9 software and manually measured the membrane potential at a post-AP peak time point (5 ms) in $Slo1^{-/-}$ and $MT_1^{-/-}$ mice, corresponding to the mean interval between the AP peak and automatically detected AHP in $Slo1^{+/+}$ mice (4.7 ms). The membrane potential in knockout mice was substantially more depolarized than the AHP in their littermate controls (**Figure 4K, Figure S3H**). This analysis underscores the essential roles of both Slo1 and MT_1 in AHP generation.

Similar changes in the AP-related parameters were observed between *Slo1* and MT_1 knockout mice and their littermate controls in both males and females. However, significant differences in the mean values of a few AP-related parameters were observed between males and females, through these differences were inconsistent between the 15-pA and 20-pA current injection steps (**Figure S3**). Overall, these findings suggest that there are no major sex-specific differences in the effects of MT_1 and *Slo1* knockout on AP-related parameters.

***Knockout of Slo1* or *MT_1 does not affect* AP duration and AHP in SCN neurons during the nighttime**

To evaluate the nighttime effects of *Slo1 or* MT_1 knockout on SCN neurons, we performed electrophysiological experiments using mice housed under a light cycle with lights on from 7:00 pm to 7:00 am and off from 7:00 am to 7:00 pm. Brain slices were prepared between 10:00 and 11:00 am and used for electrophysiological experiments between 2:00 and 5:00 pm, corresponding to ZT 15-16 and ZT 19–22, respectively.

We performed electrophysiological experiments similar to those conducted for daytime SCN neurons. Consistent with the results observed in daytime neurons, nighttime SCN neurons showed no differences in *Rm*, RMP, or the frequency of APs induced by current injection between knockout mice and their littermate controls (**Figure 5A, B**). However, unlike daytime neurons, nighttime $MT_1^{-/-}$ and $Slo1^{-/-}$ neurons did not display significant differences in any AP-related parameters compared to their littermate controls for APs induced by both 15-pA (**Figure 5**) and 20-pA (**Figure S4**) current injections, except for a significant reduction in the minimum slope in $Slo1^{-/-}$ neurons relative to $Slo1^{+/+}$ controls at 20-pA current injection (**Figure S4**).

There were no apparent sex-specific differences in the results, as indicated by the distribution of male and female data points in the bar graphs (**Figure 5 and Figure S4)**. Overall, these findings suggest that Slo1 and MT_1 do not significantly influence the AP waveform in nighttime SCN neurons, highlighting a sharp contrast to their roles in daytime SCN neuron.

We also compared AP-related parameters in SCN neurons between the daytime and nighttime within the same genotypes (knockout or littermate controls). In both $Slo1^{-/-}$ and $MT_1^{-/-}$ mice, APD_{50} was

188 significantly increased, while the minimum slope and AHP potential were significantly decreased during
189 the daytime compared to the nighttime; in contrast, their littermate controls showed no such significant
190 differences (**Figure S5**). These findings suggest that the substantial changes observed in knockout mice
191 during the daytime (**Figure 4; Figure S2**), but not the nighttime (**Figure 5; Figure S4**), arise from the
192 distinct effects of the knockout on SCN neurons between the daytime and nighttime.

193 **Slo1 expression in the SCN is elevated during the daytime and reduced at nighttime**

194 To explore the cause of the differing effects of *Slo1* and MT_1 knockout on AP properties in SCN neurons
195 between the daytime and nighttime, we performed immunohistochemistry on coronal brain slices
196 containing the SCN. Brain tissue was collected at ZT 7-8 and ZT 19–20 as daytime and nighttime samples,
197 respectively. Immunohistochemistry was performed using an antibody against the last 100 amino acid
198 residues of Slo1 (APC-021, Alomone Labs, Jerusalem, Israel). This epitope is present in three of the thirteen
199 known Slo1 isoforms in the CBA/CaJ mice (www.ensembl.org).

200 Slo1 immunoreactivity was detected in both daytime and nighttime SCN samples from $Slo1^{+/+}$ mice.
201 However, the signal in the nighttime SCN was nearly 70% weaker than that in the daytime SCN (**Figure**
202 **6**). In $Slo1^{-/-}$ mice, Slo1 immunoreactivity was also observed in the daytime SCN (**Figure 6**) but was
203 approximately 90% lower compared to daytime $Slo1^{+/+}$ samples (**Figure 6**). Although the molecular lesion
204 in $Slo1^{-/-}$ mice involves an in-frame deletion of a single exon—without directly affecting the coding
205 sequence for the antibody recognition site—Slo1 expression in the SCN was substantially reduced
206 compared to wild-type mice. This finding aligns with observations in the C57BL/6 strain, where an in-
207 frame deletion of the corresponding exon results in the loss of both Slo1 mRNA and protein in brain tissue
208 [23]. The reduction in Slo1 expression may arise from various mechanisms, such as less efficient translation
209 or reduced stability of the Slo1 mRNA or protein with the internal deletion compared to the wild-type Slo1.

210 These results suggest that Slo1 in the SCN consists primarily or exclusively of one or more isoforms
211 containing the C-terminal region recognized by the antibody. Moreover, Slo1 expression in the SCN is
212 elevated during the subjective daytime and reduced during the subjective nighttime. This substantial daily
213 variation in Slo1 expression levels may be a key factor underlying the differing effects of Slo1 knockout
214 on the electrical properties of SCN neurons between daytime and nighttime.

215 **Specific domains in MT_1 and Slo1 mediate their physical interaction**

216 We investigated whether the functional effect of MT_1 on Slo1 involves a physical interaction and whether
217 such an interaction depends on specific domains by performing co-immunoprecipitation assays. These
218 experiments were conducted with HEK293T cells transfected with MT_1 and Slo1, which were tagged at
219 their C-termini with HA and Flag, respectively. We immunoprecipitated the complexes using an HA
220 antibody and subsequently immunoblotted them using a Flag antibody.

221 We observed co-immunoprecipitation of full-length MT_1 and Slo1 (**Figure 7A-C**). To determine which
222 part of Slo1 is important for its physical interaction with MT_1, we tested whether Slo1 interacts with MT_1
223 through its N- or C-terminal domain. We observed MT_1 co-immunoprecipitation with Slo1's N-terminal
224 portion (amino acids 1-388), which includes all residues up to the end of S6, but not its C-terminal portion
225 (amino acids 389-1164), which comprises the entire cytosolic domain after S6 (**Figure 7A**). These results
226 indicate that the N-terminal portion of Slo1 mediates physical interaction with MT_1.

227 Given the importance of the S0-S1 loop of Slo1 in its activation by melatonin, we tested whether the
228 S0-S1 peptide (amino acids 44–113) itself could co-immunoprecipitate with MT_1 and observed a positive
229 result (**Figure 7B**). We then examined whether $Slo1_{\Delta S0\text{-}S1}$, where amino acids 44-113 are deleted, could still

230 interact with MT_1. $Slo1_{\Delta S0\text{-}S1}$ exhibited much weaker interaction with MT_1 compared to full-length Slo1
231 (**Figure 7C**).
232 To identify the domain in MT_1 important for physical interaction with Slo1, we tested the effects of
233 various MT_1 deletions. We observed that two MT_1 constructs, $MT_{1(1\text{-}312)}$ and $MT_{1(47\text{-}353)}$, which had the C-
234 and N-termini deleted, respectively, still coimmunoprecipitated with Slo1 (**Figure 6D**), suggesting that the
235 membrane-spanning region might be responsible for the physical interaction. To confirm this, we tested an
236 MT_1 fragment lacking both the N- and C-termini, $MT_{1(47\text{-}312)}$. This MT_1 construct still co-
237 immunoprecipitated with Slo1 (**Figure 7E**). These results suggest that the membrane-spanning region of
238 MT_1 mediates physical interaction with Slo1.
239 Since MT_2 is highly homologous to MT_1 in the membrane-spanning region, we tested whether MT_2 can
240 physically interact with Slo1. Indeed, we observed coimmunoprecipitation of MT_2 with Slo1 (**Figure 7E**).
241 The fact that both MT_1 and MT_2 physically interact with Slo1, but only MT_1 mediates melatonin activation
242 of Slo1, suggests that the distinct functional effect of MT_1 on Slo1 is not due to a distinct ability to bind to
243 Slo1.
244 Finally, we validated the specificity of our assays by testing whether MT_1 can coimmunoprecipitate
245 with an unrelated membrane protein. Specifically, we tested whether the CUB domain of human BAI3
246 (brain-specific angiogenesis inhibitor 3) with a membrane GPI anchor can coimmunoprecipitate with MT_1.
247 We were unable to detect a CUB signal in the immunoprecipitates obtained with MT_1 (**Figure 7F**). This
248 result confirms that the interactions observed between MT_1 and Slo1 are specific.

249 **Discussion**

250 This study demonstrates that knockout of Slo1 or MT_1 significantly reduces sleep duration and slows AP
251 repolarization in SCN neurons. Additionally, we show that melatonin activates Slo1 through Gβγ subunits
252 and identify key domains crucial for functional and physical interactions between MT_1 and Slo1. Given that
253 the SCN serves as the master circadian clock, these findings suggest that melatonin's sleep-promoting
254 effects are likely mediated by Slo1 activation via MT_1.
255 The use of specific knockout mice is instrumental to elucidating the roles of MT_1 and Slo1 in sleep
256 regulation. Our EEG and EMG analyses reveal that both $Slo1^{-/-}$ and $MT_1^{-/-}$ mice exhibit reduced durations
257 of REM and NREM sleep and increased wakefulness. Notably, these effects were predominantly observed
258 during the subjective daytime, when mice are less active, suggesting that Slo1 and MT_1 primarily function
259 during the day to regulate sleep. This conclusion is supported by our observation of much higher Slo1
260 expression during the day compared to the night, as well as previous findings showing that MT_1 expression
261 in the rat brain is elevated during the day [24].
262 Previous studies on $MT_1^{-/-}$ and $Slo1^{-/-}$ mice in the context of sleep behavior or circadian rhythms have
263 been limited. For $MT_1^{-/-}$, one study using the C3H/He mouse strain, which is capable of melatonin synthesis
264 [22], reported a significant reduction in REM sleep duration without affecting NREM sleep [25]. This effect was
265 more pronounced during the subjective daytime, consistent with our observations of day/night differences
266 in the impact of $MT_1^{-/-}$ on sleep. However, this study did not quantitatively compare REM sleep duration
267 between day and night. Two other studies using the C57BL/6 strain, which cannot synthesize melatonin,
268 examined the effects of $MT_1^{-/-}$ on circadian rhythms. One study found that $MT_1^{-/-}$ prevented melatonin-
269 induced phase advancement of wheel-running activity [26], while another showed that $MT_1^{-/-}$ had little effect
270 on melatonin-induced phase shift in SCN firing frequency [27]. These studies, however, provide limited

insight into the role of MT_1 in sleep behavior. For *Slo1*$^{-/-}$, no prior study has examined sleep behavior using EEG. One study using a hybrid mouse strain incapable of melatonin synthesis reported that *Slo1*$^{-/-}$ disrupts the circadian rhythm of wheel-running activity [8], but this does not directly address Slo1's role in sleep. Thus, our study provides important new insights into the roles of Slo1 and MT_1 in sleep regulation. Further research is needed to understand why the effect of *MT1*$^{-/-}$ on NREM sleep differs between the CBA/CaJ and C3H/He strains and to determine whether *Slo1*$^{-/-}$ also impairs sleep behavior in melatonin-deficient strains.

Our findings highlight the critical roles of Slo1 and MT_1 in AP repolarization and AHP generation in SCN neurons. Specifically, both *Slo1*$^{-/-}$ and *MT1*$^{-/-}$ significantly increased APD_{50} and eliminated AHP compared to littermate controls. While no previous studies have examined the effects of *MT1*$^{-/-}$ or *Slo1*$^{-/-}$ on AP waveforms in SCN neurons, two studies have investigated the effects of the Slo1 blocker iberiotoxin. One study found that iberiotoxin reduced Cd^{2+}-sensitive AHP by approximately 40% in rat SCN neurons but had no effect on AP width [28]. Another study reported that iberiotoxin increased APD_{50} by approximately 40% and reduced AHP amplitude by approximately 2 mV in young C57BL/6 mice [29]. These effects are notably weaker than those observed in our *Slo1*$^{-/-}$ experiments. The discrepancy may arise from the presence of iberiotoxin-resistant Slo1 variants in the SCN, such as those associated with the β4 subunit, which confers resistance to iberiotoxin [30]. Although knockout of the β4 subunit does not alter the circadian rhythm of SCN neuronal firing [9], it remains possible that the β4 subunit plays a role in shaping AP waveforms in SCN neurons. Alternatively, the discrepancy could result from impaired Slo1 function in the melatonin-deficient C57BL/6 strain. This possibility is supported by our findings in *C. elegans*, where SLO-1 function is compromised in the absence of melatonin secretion [15].

The observed effects of *MT1*$^{-/-}$ and *Slo1*$^{-/-}$ on SCN neuronal properties suggest the presence of either constitutively active MT_1 or locally synthesized melatonin in brain slices under our experimental conditions. As for the first possibility, studies involving inverse receptor agonists have revealed that a variety of GPCRs, including MT_1, can exhibit constitutive activity in the absence of ligands [31-33]. Although coexpression of MT_1 with Slo1 does not alter the V_{50} of Slo1 compared to Slo1 expression alone in *Xenopus* oocytes [15], this finding does not rule out the possibility that MT_1 may be constitutively active in native SCN neurons. As for the second possibility, it is unlikely that melatonin from the pineal gland would remain in brain slices after incubation in artificial cerebrospinal fluid for at least two hours prior to recording. However, previous studies suggest that melatonin may be synthesized locally in brain tissues. For example, mRNAs encoding key enzymes for melatonin synthesis, arylalkylamine *N*-acetyltransferase (AANAT) and hydroxyindole-*O*-methyltransferase (HIOMT), have been detected in various rat brain regions [34,35]. Additionally, melatonin has been detected in brain tissues of pinealectomized rats [24], with the hypothalamus showing the highest levels among the regions examined [36]. Furthermore, melatonin synthesis has been demonstrated in astrocytes, glial cells, and neural stem cells [37-39]. The K_i of melatonin for MT_1 is 0.1 nM [1,40], and we previously observed an EC_{50} of 0.77 nM for melatonin's activating effect on Slo1 via MT_1 in the *Xenopus* oocyte heterologous expression system [15]. Thus, even sub-nanomolar concentrations of melatonin in SCN slices would be sufficient to potently activate MT_1.

Neither *Slo1*$^{-/-}$ nor *MT1*$^{-/-}$ significantly altered the frequency of current injection-induced APs in SCN neurons, suggesting that Slo1 and MT_1 do not regulate sleep behavior through modulation of AP frequency. Previous studies have reported that *Slo1*$^{-/-}$ increases SCN firing rates during the subjective night [8,41]. However, these studies employed multi-electrode arrays [41] or single-unit recordings [8], techniques that are difficult to directly compare with our whole-cell recordings. Multi-electrode arrays measure the summed

activity of many neurons. Since SCN neurons are heterogenous, the neurons contributing to the elevated firing rates in the previous study [41] are likely distinct from those we recorded. Additionally, single-unit recordings in the SCN have shown high variability in firing frequencies within both *Slo1*$^{+/+}$ and *Slo1*$^{-/-}$ groups [8], necessitating the sampling of many neurons to detect significant differences—a requirement that is impractical with the whole-cell recording technique. Therefore, the absence of significant differences in AP firing rates in our study is not surprising.

In *C. elegans*, loss-of-function mutations in either a specific melatonin receptor (*pcdr-1*) or the melatonin synthesis enzyme (*homt-1*) result in sleep deficiencies similar to those caused by *slo-1* mutations [15]. These findings suggest that melatonin synthesis and PCDR-1 are required for SLO-1 function *in vivo*. In contrast, the effects of *Slo1*$^{-/-}$ on AP properties and sleep behavior were often stronger than those of *MT*$_1^{-/-}$, indicating that while MT_1 is crucial for Slo1 function, Slo1 can retain partial functionality in the absence of MT_1 in the mouse brain.

Loss-of-function mutations in *Slo1* are associated with seizures in human patients [16-18]. Consistent with these findings, we observed robust seizure activity in EEG recordings of *Slo1*$^{-/-}$ mice, which occurred between ZT5 and ZT21, with seizure activity gradually increasing during this period. Similarly, a previous study reported seizure-like locomotor behavior in *Slo1*$^{-/-}$ mice on a C57BL/6 genetic background [18]. However, another study using EEG recordings found no difference in either the latency or spectral power of pentylenetetrazol-induced seizures between wild-type and *Slo1*$^{-/-}$ mice [19]. Direct comparison of our results with those of this study is challenging, as the latter used hybrid mouse strains with an unknown capacity for melatonin synthesis and did not report any spontaneous seizures in *Slo1*$^{-/-}$ mice. The discovery of pronounced seizure phenotypes in *Slo1*$^{-/-}$ of the CBA/CaJ strain suggests that this strain could be particularly valuable for investigating the cellular and molecular mechanisms underlying seizures associated with loss-of-function mutations in Slo1.

We previously found in the *Xenopus* oocyte heterologous expression system that the Gβγ inhibitor gallein blocks the activation of human Slo1 by melatonin via MT_1. Additionally, we found that the peptidic agent mSIRK, which releases Gβγ subunits from G proteins independently of GDP-to-GTP exchange, activates human Slo1 in the absence of melatonin—but only when MT_1 is coexpressed [15]. These findings reveal that Gβγ can activate Slo1, a previously unrecognized mechanism, and suggest that melatonin activates Slo1 by releasing Gβγ subunits from G proteins associated with MT_1. The present study strengths this conclusion by providing several additional lines of evidence. These include the dependence of Slo1 activation on a G_i-type G protein, the membrane-delimited effect of melatonin on Slo1 activation, the melatonin-independent activation of Slo1 by Gβγ overexpression, and the occlusion of melatonin-induced Slo1 activation by Gβγ overexpression. Collectively, the results of these two studies provide compelling evidence that melatonin activates Slo1 by releasing free Gβγ subunits from a G_i-type G protein coupled to MT_1. This finding also resolves a conundrum regarding how Slo1 might be activated by a G_i-type G protein, as signaling through the $G_i\alpha$ subunit is typically expected to inhibit, rather than activate, the channel by reducing its phosphorylation via cAMP-dependent protein kinase A [42-44].

In summary, our findings suggest that melatonin promotes sleep by enhancing action potential (AP) repolarization in SCN neurons through MT_1-mediated activation of Slo1. This effect is facilitated by a physical interaction between MT_1 and Slo1, which we have demonstrated in this study. A key question is how the modulation of AP waveforms by MT_1 and Slo1 in SCN neurons translates into a sleep-promoting effect. Slo1 is known to be enriched at presynaptic sites, where it plays a critical role in downregulating

355 neurotransmitter release [45]. In *C. elegans*, the regulation of neurotransmitter release by SLO-1, the
356 orthologue of mammalian Slo1, depends on melatonin synthesis and the melatonin receptor PCDR-1 [15]. By
357 analogy, we propose that MT_1-dependent activation of Slo1 in the SCN may downregulate neurotransmitter
358 release from SCN neurons, thereby modulating the activity of downstream neurons to promote sleep. Future
359 studies are needed to elucidate the precise mechanisms by which MT_1 and Slo1 in the SCN interact with
360 other neural circuits to enhance sleep.

361 **ACKNOWLEDGEMENTS**

362 This work was supported by NIH grants R01MH085927 and R01NS109388 (both to Z.W.W.). The authors
363 express sincere gratitude to Xiangyou Hu and Yinyying Ge for their guidance on EEG/EMG recordings,
364 Bojun Chen for his guidance on coimmunoprecipitation assays, David Martinelli for providing the FLAG-
365 tagged CUB plasmid, Katie Lowther for her guidance on genotyping, and Riqiang Yan for providing access
366 to the confocal microscope and EEG/EMG recording system.

367 **AUTHOR CONTRIBUTIONS**

368 Z.W.W. contributed to the conception, design, interpretation of results, and manuscript writing. K.V.
369 contributed to genotyping, experimentation, and data analysis for Figures 1-3, 6, and 7, as well as
370 manuscript writing. A.A. performed the experimentation and data analysis for Figures 4, 5, and S2–S5. L.N.
371 contributed to the initial preliminary studies and provided guidance and training to A.A. in experimentation.
372 Y.S. contributed to the initial preliminary studies and assisted in training K.V. in molecular biological
373 techniques. F.L.C. guided the adoption of the slice recording technique in Z.W.W.'s lab and provided
374 troubleshooting support. X.M.M. guided the immunohistochemistry experiments. D.K. and S.P.Y. assisted
375 in maintaining and genotyping mouse strains.

376 **DECLARATION OF INTERESTS**

377 The authors declare no competing interests.

378 **METHODS DETAILS**

379 **Creation of *MT_1* and *Slo1* knockout mice**
380 *Mtnr1a (MT_1)* and *Kcnma1 (Slo1)* knockout mice were generated by the Jackson Laboratory (JAX) using
381 CRISPR-mediated gene editing of zygotes derived from CBA/CaJ mice (JAX Stock# 000654). Briefly, the
382 Benchling CRISPR Guide RNA Design Tool (https://www.benchling.com/crispr) was used to identify
383 CRISPR target sites for excising exon 1 of *MT_1* and exon 8 of *Slo1* with minimum off-target potential. The
384 following CRISPR guide RNA (crRNA) sequences were identified:
385 For *MT_1*: *MT_1*_crRNA1 (5'-GGG CCA TTG TCC TGT CGC CC) and *MT_1*_crRNA2 (5'- CTC CTG
386 GAT GAT CTT TGT CA).
387 For *Slo1*: *Slo1*_crRNA1 (5'- ATC AAG CAT CAG CGA TGC GT) and *Slo1*_crRNA2 (5'- GGC ACC
388 TGC CCC TAA AGA GC).
389 Single guide RNAs (sgRNAs) with sequences specific to *MT_1* and *Slo1* were purchased from Synthego
390 (Redwood City, CA, USA), and SpCas9 protein was obtained from Integrated DNA Technologies

(Coralville, IA, USA). These components were electroporated into zygotes following an established method.[46]

Live-born pups were initially screened by PCR using the following primer pairs:

- For *MT_1*: *MT_1*_F1 (5'-CTT GAT GCC TCC ACG TGT CT) and *MT_1*_R1 (5'-TTT TTG GCG GCT TCT GCA TC), which amplify an 827 bp fragment from the wild-type allele and a ~400 bp fragment from the knockout allele.
- For *Slo1*: *Slo1*_F1 (5'-CAA GCA GTC CCA GAA GCA GA) and *Slo1*_R1 (5'-TGA AGC AAC TGT TCC CTG GA), which amplify a 1207 bp fragment from the wild-type allele and a ~400 bp fragment from the knockout allele.

Potential founders were further confirmed by PCR followed by Sanger sequencing of the PCR products using the primers described above. Confirmed founders, including an *MT_1* allele with a 500 bp deletion and a *Slo1* allele with an 866 bp deletion and 3 bp insertion, were bred with CBA/CaJ mice to establish stable knockout lines for further characterization. The sequences, annealing sites, and PCR product sizes of oligo pairs for routine PCR genotyping are shown in Figure 1.

Mice were housed in a controlled environment with a 12-hour light/dark cycle and provided with a standard diet and water ad libitum. All experiments were conducted in accordance with the National Institutes of Health (NIH) guidelines and were approved by the Institutional Animal Care and Use Committee (IACUC) at UConn Health.

Mouse stereotaxic surgery and EEG/EMG recordings

A 12- to 14-week-old mouse was anesthetized using 2% isoflurane delivered via a gas evacuation apparatus (RWD, Gas Evacuation Apparatus R546W). The anesthetized mouse was then positioned in a stereotaxic frame equipped with a mouse adaptor (51509M, Stoelting Co., Wood Dale, IL, USA). Following exposure of the skull, an EEG/EMG head mount featuring two EEG inputs and one EMG input (8201-SS, Pinnacle Technology, Parsippany, NJ, USA) was affixed to the skull using four stainless steel screws (two anterior screws: 8209; two posterior screws: 8212; Pinnacle Technology, Parsippany, NJ, USA). The exposed skull and neck regions were subsequently covered with a ceramic dental compound (51458, Stoelting Co., Wood Dale, IL, USA).

After surgery, the mouse was allowed to recover for 7–10 days before being transferred to an EEG/EMG recording chamber. The chamber was maintained on a 12-hour light/dark cycle (lights on from 7:00 AM to 7:00 PM). The head mount was connected to a Data Acquisition and Control System (8206, Pinnacle Technology) via a preamplifier (8202-SE, Pinnacle Technology). Continuous EEG and EMG signals, along with synchronized video recordings, were acquired for 72 hours without human intervention. Data were amplified and recorded using Sirenia Acquisition software (Pinnacle Technology).

Sleep and wake duration quantification

Sleep and wake durations were quantified using the final 24 hours of EEG and EMG recordings. EEG traces were automatically segmented into 4-second epochs and classified as wake, non-rapid eye movement (NREM) sleep, or rapid eye movement (REM) sleep using a cluster scoring approach implemented in Sirenia Sleep Pro software (Pinnacle Technology). The automated classifications were manually verified by cross-referencing raw EEG/EMG data and corresponding spectral plots (power over frequency).

Wake periods were characterized by high-amplitude EMG activity and a dominant EEG frequency greater than 4 Hz. NREM sleep was identified by a dominant EEG frequency below 4 Hz and low-amplitude EMG activity. REM sleep was distinguished by a dominant EEG frequency between 5 and 8 Hz

accompanied by low-amplitude EMG signals. The total time spent in wake, NREM, and REM states during both the light and dark phases was calculated and extracted using the software.

Seizure identification and quantification

Ictal events were identified and quantified from the final 24 hours of EEG/EMG recordings in *Slo1*$^{-/-}$ mice using Sirenia Seizure Pro software (Pinnacle Technology). Ictal discharges were defined as rhythmic bursts of sharply contoured EEG activity lasting at least 10 seconds. Each event was manually selected within the EEG trace, and the total power associated with the event was quantified using Sirenia Seizure Pro. To confirm the behavioral state during each event, EMG signals and synchronized video recordings were reviewed to ensure that the mouse was awake at the time of the seizure.

Brain slice electrophysiology

Mice aged 3–5 weeks were anesthetized with 2% isoflurane and decapitated at approximately 11:00 AM. The brain was rapidly removed from the cranium and placed in an ice-cold tray containing carbogenated slicing solution (composition in mM: 125 NaCl, 2.5 KCl, 1.25 NaH_2PO_4, 26 $NaHCO_3$, 10 glucose, 10 sucrose, 0.5 $CaCl_2 \cdot 2H_2O$, and 2 $MgCl_2 \cdot 6H_2O$). The brain was then mounted on a specimen holder (VF-SPS-VM-12.5-BOS) and embedded in 2% melted agarose (A9414, Sigma) maintained at 42°C using an Eppendorf ThermoMixer F2.0. Coronal slices of 300 µm thickness were cut using an ENDURIUM® blade (EF-INZ10, Cadence, San Jose, CA, USA) on a *Compresstome* (VT-510-0Z, Precisionary Instruments LLC, Ashland, MA, USA) in ice-cold slicing solution. The entire procedure, from decapitation to obtaining brain slices, was completed within approximately 15 minutes. Slices containing the suprachiasmatic nucleus (SCN) were incubated at 37°C for 30 minutes and then maintained at room temperature in carbogenated maintenance solution (composition in mM: 125 NaCl, 2.5 KCl, 1.25 NaH_2PO_4, 26 $NaHCO_3$, 10 glucose, 10 sucrose, 2 $CaCl_2 \cdot 2H_2O$, and 4 $MgSO_4 \cdot 7H_2O$) until used for electrophysiological recordings.

SCN-containing slices were transferred to a recording chamber (RC-26G, Warner Instruments, Hamden, CT, USA) mounted on a magnetic platform (PM-1, Warner Instruments). The chamber was continuously perfused with carbogenated artificial cerebrospinal fluid (aCSF; composition in mM: 125 NaCl, 2.5 KCl, 1.25 NaH_2PO_4, 26 $NaHCO_3$, 10 glucose, 10 sucrose, 2 $CaCl_2 \cdot 2H_2O$, and 1.3 $MgCl_2 \cdot 6H_2O$), with osmolarity adjusted to 305 mOsm using sucrose. The intracellular pipette solution contained (in mM): 125 K-gluconate, 4 KCl, 0.2 $CaCl_2 \cdot 2H_2O$, 10 HEPES, 1 EGTA, 10 phosphocreatine-Na_2, 4 Na_2-ATP, and 0.3 Na-GTP, with osmolarity adjusted to 290 mOsm using sucrose.

SCN neurons were visualized using an infrared monochrome video camera (IR-2000, DAGE-MTI, Michigan City, IN, USA) under IR-DIC illumination, controlled by IR-Capture software (DAGE-MTI) on an upright microscope (Axio Examiner.Z1, Zeiss, Germany). Tear-drop or balloon-shaped neurons in the ventromedial SCN were selected for whole-cell patch-clamp recordings. Membrane resistance and capacitance were measured using the Membrane Test function, and action potentials (APs) were recorded in response to current injections. Neurons with an access resistance of <25 MΩ were selected for recording. Recordings were included for analysis only if the access resistance remained stable, increasing by no more than 10% during the experiment. Electrophysiological recordings were performed using a Multiclamp 700B amplifier, a digital-to-analog converter (Digidata 1550B), and pCLAMP software (v11, Molecular Devices, Sunnyvale, CA, USA). Data were low-pass filtered at 2 kHz and acquired at 10 kHz. Recording electrodes (tip resistance 4–6 MΩ) were pulled from borosilicate glass capillaries (BF120-69-10, Sutter Instrument, Novato, CA, USA).

474 Raw AP data files acquired using Clampex were imported into *Igor Pro 9* (WaveMetrics) for analysis.
475 For each current injection step, the software automatically quantified key parameters for individual APs,
476 including APD_{50}, maximum/minimum slopes, threshold, amplitude, AHP voltage, and the timing of AP
477 peaks and AHP occurrences. Results were exported to *Excel* to calculate average values for all APs and
478 tally the number of APs per current injection step.
479 AHP voltage for $MT_1^{+/+}$ and $Slo1^{+/+}$ mice was automatically quantified by *Igor Pro 9*, while that for
480 $MT_1^{-/-}$ and $Slo1^{-/-}$ mice was estimated using the following approach. First, the time interval between the AP
481 peak and the AHP voltage was calculated from the automatically detected times for AP peak and AHP for
482 $MT_1^{+/+}$ and $Slo1^{+/+}$ mice in *Igor Pro 9*, yielding a interval of ~5 ms. For $MT_1^{-/-}$ and $Slo1^{-/-}$ mice, AHP voltage
483 was defined as the membrane voltage measured 5 ms post-AP peak in averaged AP traces (per current
484 injection step), identified using ClampFit (Molecular Devices).

485 **Immunohistochemistry**

486 Mice were anesthetized with 2% vaporized isoflurane and subjected to transcardial perfusion. Perfusion
487 began with phosphate-buffered saline (PBS) for 5 minutes, followed by 4% paraformaldehyde (PFA) until
488 the tail stiffened and the liver turned pale, indicating proper fixation. The brain was then removed and post-
489 fixed in ice-cold 4% PFA for 2 hours. After fixation, the brain was cryoprotected by incubation in 20%
490 sucrose solution at 4°C overnight. Coronal sections of 14 μm thickness were cut using a Leica CM1860
491 UV cryostat (Leica, USA) and mounted onto gelatin-coated Superfrost microscope slides (12-550-123,
492 Fisher Scientific, USA).
493 Slides were washed three times in PBS for 5 minutes each to remove residual optimal cutting
494 temperature (OCT) compound. Sections were then blocked for 1 hour at room temperature in PBS
495 containing 5% goat serum, 1% bovine serum albumin (BSA), and 0.2% Triton X-100 (pH 7.4). After
496 blocking, sections were incubated overnight at 4°C with a 1:500 dilution of rabbit polyclonal anti-BK
497 channel antibody (APC-021, Alomone Labs, Israel). The following day, sections were washed three times
498 in PBS for 5 minutes each and incubated for 1 hour at room temperature with Alexa Fluor 594-conjugated
499 secondary antibody (Thermo Fisher Scientific, USA). After secondary antibody incubation, sections were
500 washed three more times in PBS for 5 minutes each and mounted with DAPI Fluoromount-G (Southern
501 Biotech, 0100-20, USA). Images were acquired using a Zeiss LSM 800 confocal microscope (Zeiss,
502 Germany).
503 For quantification, images were imported into ImageJ software. The scale was set using metadata
504 exported from ZEN 2.7 software (Zeiss, Germany). The bilateral suprachiasmatic nuclei (SCN) were
505 manually selected for analysis. The integrated density of the red fluorescence signal (Slo1) and the DAPI
506 signal (nuclei) were measured. The integrated density of the Slo1 signal was normalized to the
507 corresponding DAPI signal. Normalized values were exported to Origin software (OriginLab, USA) for
508 calculating the mean ± standard error (SE) and generating graphical representations.

509 **Plasmids**

510 The plasmids encoding hemagglutinin (HA)-tagged mouse MT_1 (*wp2117*) and FLAG-tagged mouse Slo1
511 (*wp2116*) were constructed by cloning PCR-amplified products into the pIRES2–EGFP vector (Clontech,
512 Mountain View, CA, USA). The *Mtnr1a* cDNA (NM_008639, MR224599, OriGene, Rockville, MD, USA)
513 and *Slo1* cDNA (MBr5/3, provided by Dr. Lawrence Salkoff's lab) were amplified using primer pairs
514 4378/4379 and 4376/4377, respectively (Table 1). The antisense primers were designed to fuse the 3'-ends
515 of the MT_1 and Slo1 coding sequences in-frame with the HA and FLAG epitope tags, respectively. The

516 resulting PCR products were cloned into the pIRES2–EGFP vector at BglII/PstI (MT_1) and KpnI/BamHI
517 (Slo1) restriction sites.
518 To generate plasmids encoding HA-tagged MT_1(1-312) (*wp2144*) and FLAG-tagged Slo1(1-388)
519 (*wp2138*), the corresponding cDNA fragments were amplified using primer pairs 4378/4433 and 4397/4419,
520 respectively (Table 1). The antisense primers 4433 and 4419 were designed to fuse the codons for amino
521 acids 312 (MT_1) and 388 (Slo1) in-frame with the HA and FLAG tags, respectively. The amplified products
522 were cloned into the pIRES2-EGFP vector at BglII/PstI (MT_1) and SalI/BamHI (Slo1) restriction sites.
523 Plasmids encoding HA-tagged MT_1(47-353) (*wp2143*) and FLAG-tagged Slo1(389-1164) (*wp2139)*
524 were generated by amplifying the corresponding cDNA fragments using primer pairs 4432/4379 and
525 4420/4377, respectively (Table 1). The sense primers 4432 and 4420 included start codons (ATG). The
526 amplified products were cloned into the pIRES2-EGFP vector at BglII/PstI (MT_1) and SalI/BamHI (Slo1)
527 restriction sites. The plasmid encoding HA-tagged MT_1(47-312) (*wp2151)* was generated by amplifying
528 the corresponding cDNA fragment using primer pair 4432/4433, where the sense primer 4432 included a
529 start codon (ATG) and the antisense primer 4433 introduced a premature stop codon. The amplified product
530 was cloned into the pIRES2-EGFP vector at BglII/PstI restriction sites.
531 The plasmid encoding FLAG-tagged Slo1(44-113) (*wp2152)* was generated by amplifying
532 the *Slo1* cDNA using primer pair 4478/4479, with a methionine codon added before the codon for amino
533 acid 44. The antisense primer fused the codon for amino acid 113 in-frame with the FLAG tag. The PCR
534 product was cloned into the pIRES2–EGFP vector at BglII/BamHI sites. The FLAG-tagged Slo1(Δ44-113)
535 plasmid was constructed using the Hi-Fi DNA Assembly kit (E2621S, New England Biolabs, Ipswich, MA,
536 USA). Two PCR products, amplified using primer pairs 4766/4668 and 4667/4746, were assembled with
537 SalI/HindIII-digested plasmid (*wp2116*). The antisense primer 4668 and the sense primer 4667 were
538 complementary to the *Slo1* cDNA sequence but excluded the coding nucleotides for amino acids 44-113.
539 The plasmid encoding FLAG-tagged CUB (*wp2118)* was a gift from Dr. David Martinelli [47].

540 **Coimmunoprecipitation**

541 Human embryonic kidney (HEK) 293T cells were cultured in Dulbecco's Modified Eagle Medium (DMEM)
542 supplemented with 10% fetal bovine serum (FBS). Transient transfection with hemagglutinin (HA)-tagged
543 mouse MTNR1A and FLAG-tagged mouse Slo1 (MBr5/3) and their various deletion constructs were
544 carried out was performed using Lipofectamine™ 2000 transfection reagent (Invitrogen) according to the
545 manufacturer's instructions. Cells were harvested 48 hours post-transfection and lysed in 1% CHAPS buffer
546 (75621-03-03, Fisher BioReagents) supplemented with a protease inhibitor cocktail (Roche, Basel,
547 Switzerland), with the pH adjusted to 6.8. Lysates were centrifuged at 16,000 rpm for 15 minutes to remove
548 cellular debris.
549 Supernatants were incubated with Pierce™ anti-HA magnetic beads (Thermo Fisher Scientific) for 30
550 minutes at room temperature with gentle rotation. The magnetic beads were collected using a Magna GrIP
551 rack (20-400, Millipore, Jaffrey, NH, USA) and washed twice with 1X TBST buffer (20 mM Tris, pH 7.6,
552 150 mM NaCl, 0.1% Tween-20) and once with ultrapure distilled water (10977015, Invitrogen, Carlsbad,
553 CA, USA). Immunoprecipitated proteins were eluted from the beads by incubation with 1X SDS loading
554 buffer for 10 minutes at 37°C. The eluted proteins were then resolved by SDS/PAGE and analyzed by
555 immunoblotting

556 **Western blot**

557 Immunoprecipitated proteins were resolved by electrophoresis on an SDS-PAGE gel (Invitrogen, USA) and
558 transferred onto a 0.22 μm PVDF membrane (Millipore, USA) under ice-cold conditions at 200 mA for 3

559 hours. Following transfer, the membrane was blocked with 5% non-fat milk in 1X TBST buffer (20 mM
560 Tris, pH 7.6, 150 mM NaCl, 0.1% Tween-20) for 30 minutes at room temperature. The membrane was then
561 incubated with the appropriate primary antibody overnight at 4°C.
562 The next day, the membrane was washed three times with TBST buffer for 5 minutes each and incubated
563 with the corresponding horseradish peroxidase (HRP)-conjugated secondary antibody at room temperature
564 for 1 hour. Protein signals were visualized using a ChemiDoc Imaging System (Bio-Rad, Hercules, CA).

565 **Antibodies and Reagents**

566 The following primary and secondary antibodies were used for immunoblotting:

567 - Rabbit monoclonal anti-FLAG antibody (SAB4301135, Sigma) at a dilution of 1:2000.
568 - Mouse monoclonal anti-HA antibody (sc-7392, Santa Cruz Biotechnology, Dallas, TX, USA) at a
569 dilution of 1:1000.
570 - Horseradish peroxidase (HRP)-conjugated goat anti-rabbit IgG (sc-2004, Santa Cruz
571 Biotechnology) at a dilution of 1:10,000.
572 - HRP-conjugated goat anti-mouse IgG (sc-2005, Santa Cruz Biotechnology) at a dilution of
573 1:10,000.

574 **Statistical analysis**

575 Experimental results are expressed as mean ± standard error (SE). Data graphing and statistical analyses
576 were performed using OriginPro software (OriginLab, Northampton, MA, USA). Specific statistical
577 methods used for each analysis are detailed in the corresponding figure legends.

578 **Table 1. List of primers**

Primer ID	Primer Sequence (5'- 3')
4376	AGTGGTACCATGGATGCGCTCATCATACCG
4377	ATTGGATCCTTACTTGTCGTCATCGTCTTTGTAGTCACATTCAT CTTCAACTTCTCTGA
4378	AGTAGATCTACCATGAAGGGCAATGTCAGCGAGC
4379	AGTCTGCAGTTAAGCGTAGTCTGGGACGTCGTATGGGTATAC AACAGAGTCCACCTTTAT
4397	ATTGTCGACCATGGATGCGCTCATCATACCG
4419	ATTGGATCCTTACTTGTCGTCATCGTCTTTGTAGTCCTCAAGC TCAAGGTTAGGGG
4420	ATTGTCGACCATGGCTCTGTTCAAACGGCATTTC
4432	ATTAGATCTACCATGGGCAACCTGCTGGTCATCCTGT
4433	ATTCTGCAGTTAAGCGTAGTCTGGGACGTCGTATGGGTATACA ATCTTTTTGTATTCCTTTCTGA
4478	ATTAGATCTACCATGCGGACGCTCAAGTACCTGTG
4479	ATTGGATCCTTACTTGTCGTCATCGTCTTTGTAGTCTCTGCCA GTCAGTGTCTGGGC
4667	TTGCTCTGGCGGACGATGACATCTGTGAAGGACTGGGC
4668	CTTCACAGATGTCATCGTCCGCCAGAGCAA
4746	GCTATCATCAGGAGCTTAAG
4766	ATCGATCCCAAGTCGACACGATG

579

580 **REFERENCES**

581 1. Dubocovich, M.L., Delagrange, P., Krause, D.N., Sugden, D., Cardinali, D.P., and Olcese, J. (2010).
582 International Union of Basic and Clinical Pharmacology. LXXV. Nomenclature, classification, and
583 pharmacology of G protein-coupled melatonin receptors. Pharmacol Rev *62*, 343-380.
584 10.1124/pr.110.002832.

585 2. Hastings, M.H., Maywood, E.S., and Brancaccio, M. (2018). Generation of circadian rhythms in the
586 suprachiasmatic nucleus. Nat Rev Neurosci *19*, 453-469. 10.1038/s41583-018-0026-z.

587 3. Dibner, C., Schibler, U., and Albrecht, U. (2010). The mammalian circadian timing system:
588 organization and coordination of central and peripheral clocks. Annu Rev Physiol *72*, 517-549.
589 10.1146/annurev-physiol-021909-135821.

590 4. Saper, C.B., Fuller, P.M., Pedersen, N.P., Lu, J., and Scammell, T.E. (2010). Sleep state switching.
591 Neuron *68*, 1023-1042. 10.1016/j.neuron.2010.11.032.

592 5. Saper, C.B., Scammell, T.E., and Lu, J. (2005). Hypothalamic regulation of sleep and circadian
593 rhythms. Nature *437*, 1257-1263. 10.1038/nature04284.

594 6. Harvey, J.R.M., Plante, A.E., and Meredith, A.L. (2020). Ion Channels Controlling Circadian
595 Rhythms in Suprachiasmatic Nucleus Excitability. Physiol Rev *100*, 1415-1454.
596 10.1152/physrev.00027.2019.

597 7. Salkoff, L., Butler, A., Ferreira, G., Santi, C., and Wei, A. (2006). High-conductance potassium
598 channels of the SLO family. Nat Rev Neurosci *7*, 921-931.

599 8. Meredith, A.L., Wiler, S.W., Miller, B.H., Takahashi, J.S., Fodor, A.A., Ruby, N.F., and Aldrich, R.W.
600 (2006). BK calcium-activated potassium channels regulate circadian behavioral rhythms and
601 pacemaker output. Nat Neurosci *9*, 1041-1049. 10.1038/nn1740.

602 9. Whitt, J.P., Montgomery, J.R., and Meredith, A.L. (2016). BK channel inactivation gates daytime
603 excitability in the circadian clock. Nat Commun *7*, 10837. 10.1038/ncomms10837.

604 10. Pitts, G.R., Ohta, H., and McMahon, D.G. (2006). Daily rhythmicity of large-conductance Ca2+ -
605 activated K+ currents in suprachiasmatic nucleus neurons. Brain Res *1071*, 54-62.
606 10.1016/j.brainres.2005.11.078.

607 11. Lacoste, B., Angeloni, D., Dominguez-Lopez, S., Calderoni, S., Mauro, A., Fraschini, F., Descarries,
608 L., and Gobbi, G. (2015). Anatomical and cellular localization of melatonin MT1 and MT2 receptors
609 in the adult rat brain. J Pineal Res *58*, 397-417. 10.1111/jpi.12224.

610 12. Sugden, D., McArthur, A.J., Ajpru, S., Duniec, K., and Piggins, H.D. (1999). Expression of mt(1)
611 melatonin receptor subtype mRNA in the entrained rat suprachiasmatic nucleus: a quantitative RT-
612 PCR study across the diurnal cycle. Brain Res Mol Brain Res *72*, 176-182. 10.1016/s0169-
613 328x(99)00222-3.

614 13. Waly, N.E., and Hallworth, R. (2015). Circadian Pattern of Melatonin MT1 and MT2 Receptor
615 Localization in the Rat Suprachiasmatic Nucleus. J Circadian Rhythms *13*, 1. 10.5334/jcr.ab.

616 14. Montgomery, J.R., Whitt, J.P., Wright, B.N., Lai, M.H., and Meredith, A.L. (2013). Mis-expression of
617 the BK K(+) channel disrupts suprachiasmatic nucleus circuit rhythmicity and alters clock-controlled
618 behavior. Am J Physiol Cell Physiol *304*, C299-311. 10.1152/ajpcell.00302.2012.

619 15. Niu, L., Li, Y., Zong, P., Liu, P., Shui, Y., Chen, B., and Wang, Z.W. (2020). Melatonin promotes sleep
620 by activating the BK channel in *C. elegans*. Proc Natl Acad Sci U S A *117*, 25128-25137.
621 10.1073/pnas.2010928117.

16. Tabarki, B., AlMajhad, N., AlHashem, A., Shaheen, R., and Alkuraya, F.S. (2016). Homozygous KCNMA1 mutation as a cause of cerebellar atrophy, developmental delay and seizures. Hum Genet *135*, 1295-1298. 10.1007/s00439-016-1726-y.

17. Liang, L., Li, X., Moutton, S., Schrier Vergano, S.A., Cogne, B., Saint-Martin, A., Hurst, A.C.E., Hu, Y., Bodamer, O., Thevenon, J., et al. (2019). De novo loss-of-function KCNMA1 variants are associated with a new multiple malformation syndrome and a broad spectrum of developmental and neurological phenotypes. Hum Mol Genet *28*, 2937-2951. 10.1093/hmg/ddz117.

18. Yao, Y., Qu, D., Jing, X., Jia, Y., Zhong, Q., Zhuo, L., Chen, X., Li, G., Tang, L., Zhu, Y., et al. (2021). Molecular Mechanisms of Epileptic Encephalopathy Caused by KCNMA1 Loss-of-Function Mutations. Front Pharmacol *12*, 775328. 10.3389/fphar.2021.775328.

19. Park, S.M., Roache, C.E., Iffland, P.H., 2nd, Moldenhauer, H.J., Matychak, K.K., Plante, A.E., Lieberman, A.G., Crino, P.B., and Meredith, A. (2022). BK channel properties correlate with neurobehavioral severity in three KCNMA1-linked channelopathy mouse models. Elife *11*. 10.7554/eLife.77953.

20. Ebihara, S., Marks, T., Hudson, D.J., and Menaker, M. (1986). Genetic control of melatonin synthesis in the pineal gland of the mouse. Science *231*, 491-493. 10.1126/science.3941912.

21. Roseboom, P.H., Namboodiri, M.A., Zimonjic, D.B., Popescu, N.C., Rodriguez, I.R., Gastel, J.A., and Klein, D.C. (1998). Natural melatonin 'knockdown' in C57BL/6J mice: rare mechanism truncates serotonin N-acetyltransferase. Brain Res Mol Brain Res *63*, 189-197. 10.1016/s0169-328x(98)00273-3.

22. Kasahara, T., Abe, K., Mekada, K., Yoshiki, A., and Kato, T. (2010). Genetic variation of melatonin productivity in laboratory mice under domestication. Proc Natl Acad Sci U S A *107*, 6412-6417. 10.1073/pnas.0914399107.

23. Sausbier, M., Hu, H., Arntz, C., Feil, S., Kamm, S., Adelsberger, H., Sausbier, U., Sailer, C.A., Feil, R., Hofmann, F., et al. (2004). Cerebellar ataxia and Purkinje cell dysfunction caused by Ca2+-activated K+ channel deficiency. Proc Natl Acad Sci U S A *101*, 9474-9478.

24. Jimenez-Jorge, S., Guerrero, J.M., Jimenez-Caliani, A.J., Naranjo, M.C., Lardone, P.J., Carrillo-Vico, A., Osuna, C., and Molinero, P. (2007). Evidence for melatonin synthesis in the rat brain during development. J Pineal Res *42*, 240-246. 10.1111/j.1600-079X.2006.00411.x.

25. Comai, S., Ochoa-Sanchez, R., and Gobbi, G. (2013). Sleep-wake characterization of double MT(1)/MT(2) receptor knockout mice and comparison with MT(1) and MT(2) receptor knockout mice. Behav Brain Res *243*, 231-238. 10.1016/j.bbr.2013.01.008.

26. Dubocovich, M.L., Hudson, R.L., Sumaya, I.C., Masana, M.I., and Manna, E. (2005). Effect of MT1 melatonin receptor deletion on melatonin-mediated phase shift of circadian rhythms in the C57BL/6 mouse. J Pineal Res *39*, 113-120. 10.1111/j.1600-079X.2005.00230.x.

27. Liu, C., Weaver, D.R., Jin, X., Shearman, L.P., Pieschl, R.L., Gribkoff, V.K., and Reppert, S.M. (1997). Molecular dissection of two distinct actions of melatonin on the suprachiasmatic circadian clock. Neuron *19*, 91-102. 10.1016/s0896-6273(00)80350-5.

28. Cloues, R.K., and Sather, W.A. (2003). Afterhyperpolarization regulates firing rate in neurons of the suprachiasmatic nucleus. J Neurosci *23*, 1593-1604. 10.1523/JNEUROSCI.23-05-01593.2003.

29. Farajnia, S., Meijer, J.H., and Michel, S. (2015). Age-related changes in large-conductance calcium-activated potassium channels in mammalian circadian clock neurons. Neurobiol Aging *36*, 2176-2183. 10.1016/j.neurobiolaging.2014.12.040.

30. Meera, P., Wallner, M., and Toro, L. (2000). A neuronal beta subunit (KCNMB4) makes the large conductance, voltage- and Ca^{2+}-activated K^+ channel resistant to charybdotoxin and iberiotoxin. Proc Natl Acad Sci U S A *97*, 5562-5567.

31. Milligan, G. (2003). Constitutive activity and inverse agonists of G protein-coupled receptors: a current perspective. Mol Pharmacol *64*, 1271-1276. 10.1124/mol.64.6.1271.

32. Kenakin, T. (2004). Efficacy as a vector: the relative prevalence and paucity of inverse agonism. Mol Pharmacol *65*, 2-11. 10.1124/mol.65.1.2.

33. Ersahin, C., Masana, M.I., and Dubocovich, M.L. (2002). Constitutively active melatonin MT(1) receptors in male rat caudal arteries. Eur J Pharmacol *439*, 171-172. 10.1016/s0014-2999(02)01407-3.

34. Stefulj, J., Hortner, M., Ghosh, M., Schauenstein, K., Rinner, I., Wolfler, A., Semmler, J., and Liebmann, P.M. (2001). Gene expression of the key enzymes of melatonin synthesis in extrapineal tissues of the rat. J Pineal Res *30*, 243-247. 10.1034/j.1600-079x.2001.300408.x.

35. Uz, T., Qu, T., Sugaya, K., and Manev, H. (2002). Neuronal expression of arylalkylamine N-acetyltransferase (AANAT) mRNA in the rat brain. Neurosci Res *42*, 309-316. 10.1016/s0168-0102(02)00011-1.

36. Pang, S.F., and Brown, G.M. (1983). Regional concentrations of melatonin in the rat brain in the light and dark period. Life Sci *33*, 1199-1204. 10.1016/0024-3205(83)90025-5.

37. Acuna-Castroviejo, D., Escames, G., Venegas, C., Diaz-Casado, M.E., Lima-Cabello, E., Lopez, L.C., Rosales-Corral, S., Tan, D.X., and Reiter, R.J. (2014). Extrapineal melatonin: sources, regulation, and potential functions. Cell Mol Life Sci *71*, 2997-3025. 10.1007/s00018-014-1579-2.

38. Liu, Y.J., Zhuang, J., Zhu, H.Y., Shen, Y.X., Tan, Z.L., and Zhou, J.N. (2007). Cultured rat cortical astrocytes synthesize melatonin: absence of a diurnal rhythm. J Pineal Res *43*, 232-238. 10.1111/j.1600-079X.2007.00466.x.

39. Tan, D.X., Manchester, L.C., Sanchez-Barcelo, E., Mediavilla, M.D., and Reiter, R.J. (2010). Significance of high levels of endogenous melatonin in Mammalian cerebrospinal fluid and in the central nervous system. Curr Neuropharmacol *8*, 162-167. 10.2174/157015910792246182.

40. Gobbi, G., and Comai, S. (2019). Differential Function of Melatonin MT(1) and MT(2) Receptors in REM and NREM Sleep. Front Endocrinol (Lausanne) *10*, 87. 10.3389/fendo.2019.00087.

41. Kent, J., and Meredith, A.L. (2008). BK channels regulate spontaneous action potential rhythmicity in the suprachiasmatic nucleus. PLoS One *3*, e3884. 10.1371/journal.pone.0003884.

42. Tian, L., Coghill, L.S., McClafferty, H., MacDonald, S.H., Antoni, F.A., Ruth, P., Knaus, H.G., and Shipston, M.J. (2004). Distinct stoichiometry of BKCa channel tetramer phosphorylation specifies channel activation and inhibition by cAMP-dependent protein kinase. Proc Natl Acad Sci U S A *101*, 11897-11902. 10.1073/pnas.0402590101.

43. Widmer, H.A., Rowe, I.C., and Shipston, M.J. (2003). Conditional protein phosphorylation regulates BK channel activity in rat cerebellar Purkinje neurons. J Physiol *552*, 379-391. 10.1113/jphysiol.2003.046441.

44. Nara, M., Dhulipala, P.D., Wang, Y.X., and Kotlikoff, M.I. (1998). Reconstitution of beta-adrenergic modulation of large conductance, calcium-activated potassium (maxi-K) channels in Xenopus oocytes. Identification of the camp-dependent protein kinase phosphorylation site. J Biol Chem *273*, 14920-14924.

45. Wang, Z.W., Trussell, L.O., and Vedantham, K. (2023). Regulation of Neurotransmitter Release by K(+) Channels. Adv Neurobiol *33*, 305-331. 10.1007/978-3-031-34229-5_12.

46. Qin, W., Dion, S.L., Kutny, P.M., Zhang, Y., Cheng, A.W., Jillette, N.L., Malhotra, A., Geurts, A.M., Chen, Y.G., and Wang, H. (2015). Efficient CRISPR/Cas9-Mediated Genome Editing in Mice by Zygote Electroporation of Nuclease. Genetics *200*, 423-430. 10.1534/genetics.115.176594.

47. Sticco, M.J., Pena Palomino, P.A., Lukacsovich, D., Thompson, B.L., Foldy, C., Ressl, S., and Martinelli, D.C. (2021). C1QL3 promotes cell-cell adhesion by mediating complex formation between ADGRB3/BAI3 and neuronal pentraxins. FASEB J *35*, e21194. 10.1096/fj.202000351RR.

716 **FIGURE LEGENDS**

717 **Figure 1: Generation of $MT_1^{-/-}$ and $Slo1^{-/-}$ mice**
718 (A) Schematic representation of the *Mtnr1a* (MT_1) gene, indicating the location and size of the deletion.
719 (B) Schematic diagram of PCR primers used for genotyping, with the expected PCR product sizes for
720 $MT_1^{+/+}$, $MT_1^{+/-}$ *and* $MT_1^{-/-}$ provided in the table.
721 (C) Gel image showing PCR genotyping results for $MT_1^{+/+}$, $MT_1^{+/-}$ *and* $MT_1^{-/-}$ mice.
722 (D) Schematic representation of the *Kcnma1* (*Slo1*) gene, indicating the location and size of the deletion,
723 and an α-helical representation of Slo1 highlighting the deleted amino acids within the core structure of the
724 channel.
725 (E) Schematic diagram of PCR primers used for genotyping, with the expected PCR product sizes for
726 $Slo1^{+/+}$, $Slo1^{+/-}$ *and* $Slo1^{-/-}$ provided in the table.
727 (F) Gel image showing PCR genotyping results for $Slo1^{+/+}$, $Slo1^{+/-}$ *and* $Slo1^{-/-}$ mice.
728

729 **Figure 2. $Slo1^{-/-}$ and $MT_1^{-/-}$ mice exhibit reduced REM and NREM sleep and increased wakefulness**
730 **primarily during the subjective daytime.**
731 (A) Representative traces of electroencephalogram (EEG) and electromyogram (EMG) showing
732 distinguishing features of REM sleep, NREM sleep, and wakefulness.
733 (B) Representative hypnograms derived from EEG and EMG recordings for $Slo1^{+/+}$, $Slo1^{-/-}$, $MT_1^{+/+}$, and
734 $MT_1^{-/-}$ mice.
735 (C) Quantification of sleep and wake durations during the subjective daytime.
736 (D) Quantification of sleep and wake durations during the subjective nighttime.
737 In panels C and D, the sample size (*n*) was 6 per group, including three males (blue data points) and three
738 females (red data points). Asterisks indicate statistically significant differences between knockout mice and
739 their corresponding littermate controls (* $p < 0.05$; ** $p < 0.01$; *** $p < 0.001$), while pound symbols
740 indicate significant differences between $Slo1^{+/+}$ and $MT_1^{+/+}$ or between $Slo1^{-/-}$ and $MT_1^{-/-}$ (# $p < 0.05$; ## p
741 < 0.01). Statistical analyses were performed using one-way *ANOVA* followed by Tukey's post hoc test.

742 **Figure 3: $Slo1^{-/-}$ mice exhibit seizure activity.**
743 (A) Representative electroencephalogram (EEG) traces from $Slo1^{+/+}$ and $Slo1^{-/-}$ mice.
744 (B) Comparison of cumulative EEG power between $Slo1^{+/+}$ and $Slo1^{-/-}$ mice. For $Slo1^{-/-}$ mice, cumulative
745 EEG power was calculated as the sum of the total power of all seizure events. For $Slo1^{+/+}$ mice, which
746 exhibited no seizure activity, cumulative EEG power was calculated as the sum of the total power of
747 randomly selected EEG segments. These segments matched the mean number (18) and mean duration
748 (17.6 seconds) of seizure events observed in the $Slo1^{-/-}$ group.
749 (C) Comparison of cumulative EEG power between Slo1+/+ and $Slo1^{-/-}$ mice, analyzed based on Zeitgeber
750 time (ZT) and grouped into 4-hour intervals.
751 In (B) and (C), the sample size (n) was 6 per genotype, including three males (blue data points) and three
752 females (red data points). Statistical significance (***, $p < 0.001$) between $Slo1^{-/-}$ mice and their littermate
753 controls was determined using an unpaired t-test in (B) and a two-way mixed-design ANOVA followed by
754 Tukey's post hoc test in (C).

755 **Figure 4. SCN neurons in $Slo1^{-/-}$ and $MT_1^{-/-}$ mice exhibit prolonged action potential (AP) duration and**
756 **suppressed afterhyperpolarization (AHP) during the subjective day.**

(A) Membrane resistance (R_m) and resting membrane potential (RMP) are unaffected by *Slo1*$^{-/-}$ or *MT1*$^{-/-}$.
(B) *Slo1*$^{-/-}$ or *MT1*$^{-/-}$ does not alter the frequency of APs induced by current injections. *Left*: Diagram of the current injection protocol. *Middle*: Representative current-clamp traces during 15-pA current injection. *Right*: AP frequency as a function of current injection. Filled and open triangles indicate statistically significant differences compared to the AP frequency at 0-pA current injection for the same group ($\Delta\, p < 0.05$; $\Delta\Delta\, p < 0.01$; $\Delta\Delta\Delta\, p < 0.001$). Statistical analyses were performed using two-way mixed-design *ANOVA* followed by Tukey's post hoc test.
(C) Representative AP trace illustrating the quantification of AP threshold (TH), AP amplitude, APD_{50} (AP duration at 50% repolarization), and AHP.
(D) Voltage phase plots of group averaged APs induced by 15-pA current injection. Blue arrows indicate TH, AP peak, and maximum and minimum slopes.
(E) Group-averaged APs induced by 15-pA current injection, displayed as actual (left) and normalized (right) waveforms.
(F-K). Quantitative comparisons of AP-related parameters. Asterisks indicate statistically significant differences between groups (* $p < 0.05$; ** $p < 0.01$; *** $p < 0.001$), while "ns" indicates no significant difference. Statistical analyses were performed using two-way *ANOVA* (factors: genotype and time of day) followed by Tukey's post hoc test. The number of neurons recorded (n) were: *Slo1*$^{+/+}$ 16, *Slo1*$^{-/-}$ 12, *MT1*$^{+/+}$ 11, *MT1*$^{-/-}$ 21, and *MT1*$^{-/-}$;*Slo1*$^{-/-}$ double knockout (DKO) 19.

Figure 5. *Slo1*$^{-/-}$ or *MT1*$^{-/-}$ does not alter action potential (AP) duration in SCN neurons during the subjective night.
(A) Membrane resistance (R_m) and resting membrane potential (RMP) are unaffected by *Slo1*$^{-/-}$ or *MT1*$^{-/-}$.
(B) *Slo1*$^{-/-}$ or *MT1*$^{-/-}$ does not alter the frequency of APs induced by current injections. *Left*: Diagram of the current injection protocol. *Middle*: Representative current-clamp traces during 15-pA current injection. *Right*: AP frequency as a function of current injection. Filled and open triangles indicate statistically significant differences compared to the AP frequency at 0-pA current injection for the same group ($\Delta\, p < 0.05$; $\Delta\Delta\, p < 0.01$; $\Delta\Delta\Delta\, p < 0.001$). Statistical analyses were performed using two-way mixed-design *ANOVA* followed by Tukey's post hoc test.
(C) Voltage phase plots of group averaged APs induced by 15-pA current injection.
(D) Group-averaged APs induced by 15-pA current injection, displayed as actual (left) and normalized (right) waveforms.
(E-J). Quantitative comparisons of AP-related parameters. Asterisks indicate statistically significant differences between groups (* $p < 0.05$; *** $p < 0.001$), while "ns" indicates no significant difference. Statistical analyses were performed using two-way *ANOVA* (factors: genotype and time of day) followed by Tukey's post hoc test. The number of neurons recorded (n) were: *Slo1*$^{+/+}$ 15, *Slo1*$^{-/-}$ 19, *MT1*$^{+/+}$ 16, and *MT1*$^{-/-}$ 18.

Figure 6. Slo1 expression in the SCN is elevated during the subjective day and reduced during the subjective night.
(A) Representative immunohistochemistry images showing Slo1 immunoreactivity, DAPI staining, and merged images of the two in the bilateral SCN at ZT7 and ZT9 for Slo1+/+ and at ZT7 for Slo1-/-.
(B) Quantification of Slo1 immunoreactivity across groups. Asterisks indicate statistically significant differences between groups (** $p < 0.01$; *** $p < 0.001$). Statistical analyses were performed using one-

way *ANOVA* followed by Tukey's post hoc test. The sample size (*n*) was 3 animals per group, with the Slo1 immunoreactive signal (normalized to DAPI signal) for each animal derived from the average of five sections.

Figure 7. MT_1 and Slo1 physically interact, with the membrane-spanning region of MT_1 and the S0-S1 loop of Slo1 being critical for the interaction.

Potential physical interactions between MT_1 and Slo1 were explored using coimmunoprecipitation assays with HEK293T cells transfected HA-tagged MT_1 (MT_1::HA) and Flag-tagged Slo1 (Slo1::Flag) or their variants.

(A) Full-length Slo1 and Slo1(1-388), but not Slo1(389-1164), coimmunoprecipitated with MT_1.

(B) Slo1(Δ44-113), which lacks a large portion of the S0-S1 loop, exhibited a much weaker interaction MT_1 compared to full-length Slo1.

(C) The Slo1(44-113) peptide coimmunoprecipitated with MT_1.

(D) Both MT_1(Δ1-46) and MT_1(Δ313-353), which lack the N- and C-termini, respectively, coimmunoprecipitated with Slo1.

(E) MT_1(47-312), which lacks both the N- and C-termini, as well as MT_2, coimmunoprecipitated with Slo1.

(F) An unrelated transmembrane protein, CUB3, did not coimmunoprecipitate with MT_1.

Each gel image is representative of two independent experiments.

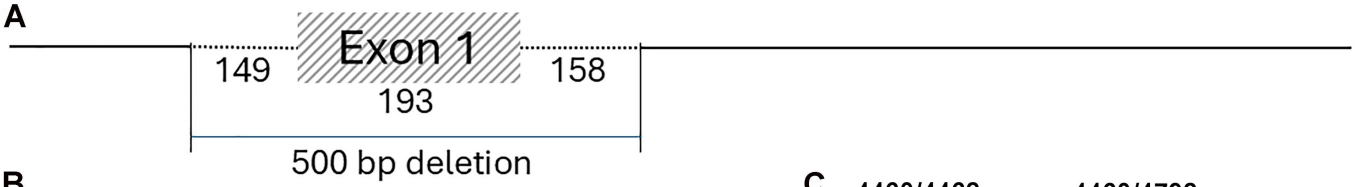

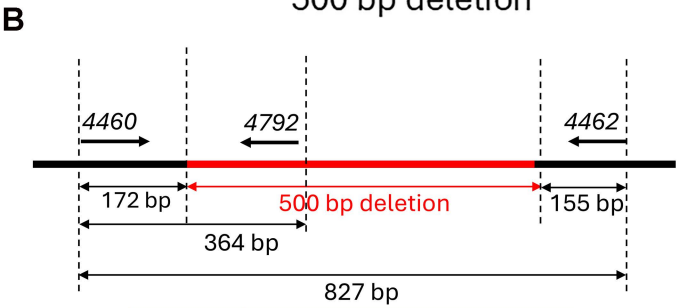

Primer Pair	Genotype		
	+/+	+/-	-/-
4460/4462	827 bp	827, 327 bp	327 bp
4460/4792	364 bp	364 bp	No band

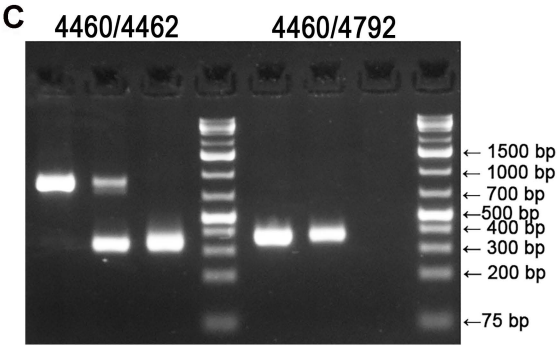

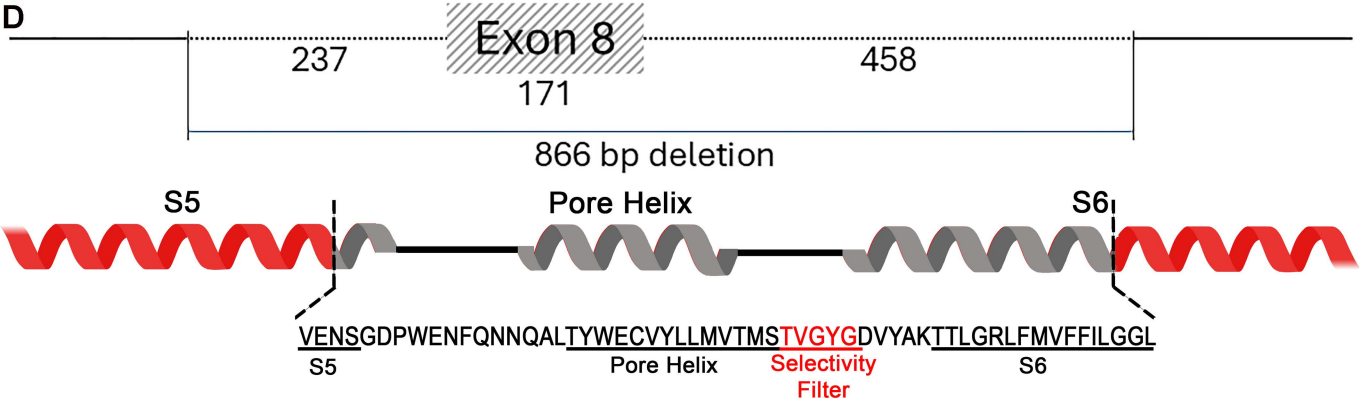

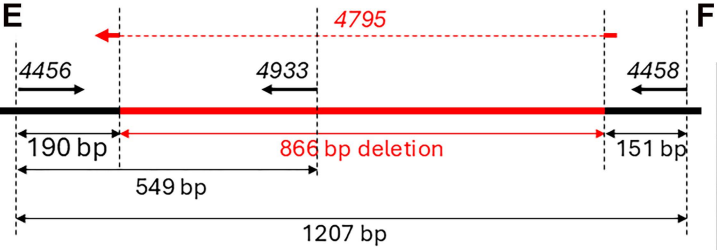

Primer Pair	Genotype		
	+/+	+/-	-/-
4456/4458	1207 bp	1207, 344 bp	344 bp
4456/4933	549 bp	549 bp	No band
4456/4975	No band	201 bp	201 bp

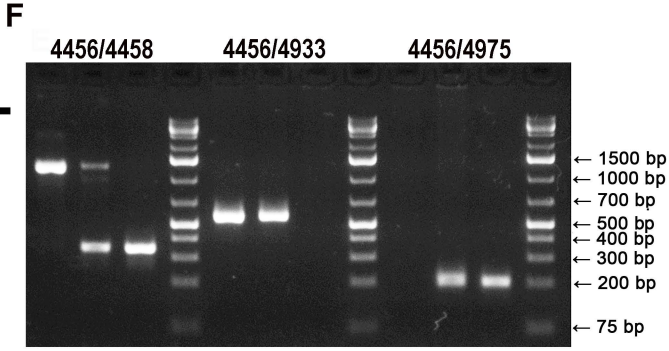

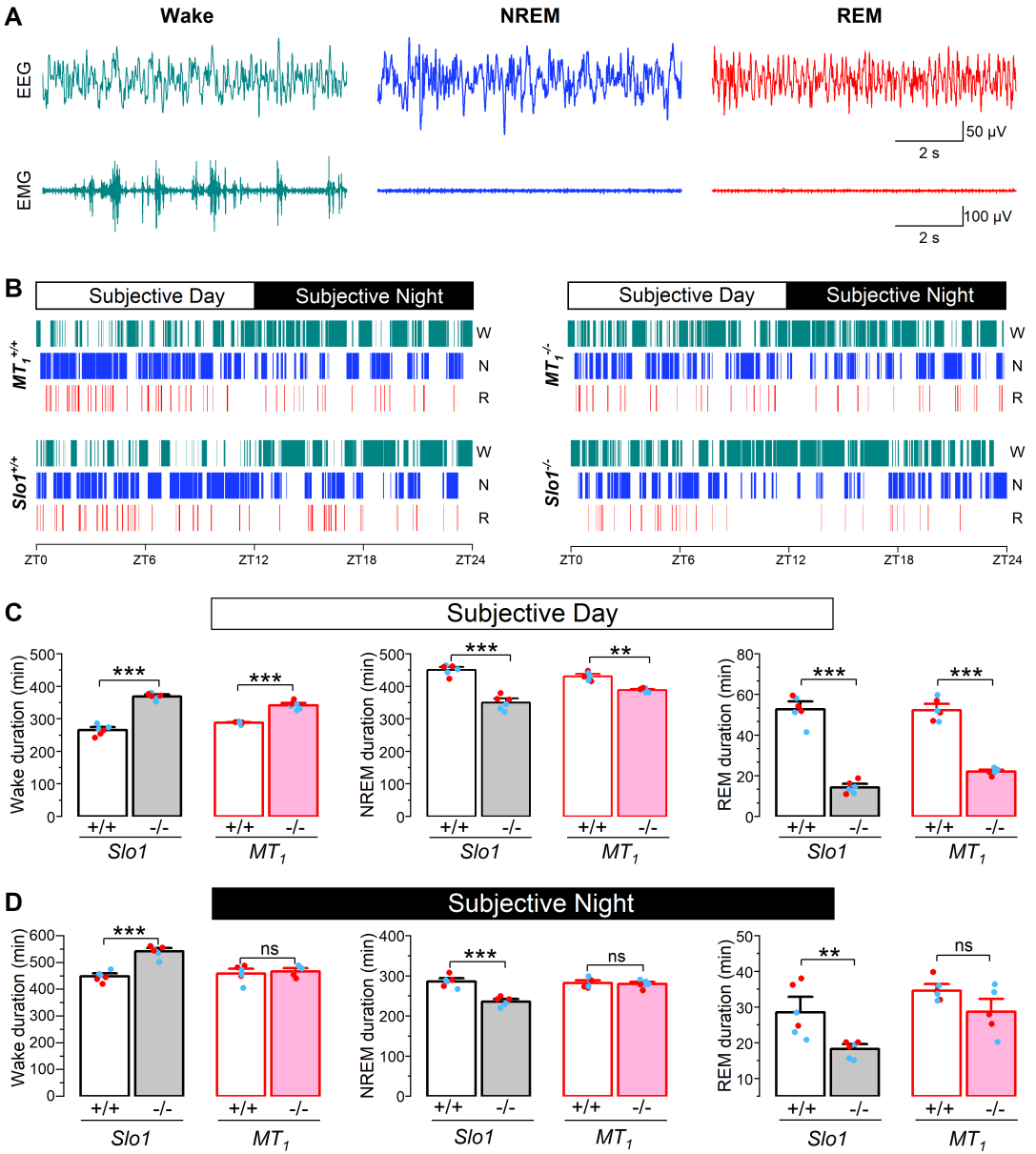
A
Wake
NREM
REM
EEG
EMG
50 µV
2 s
100 µV
2 s
B
Subjective Day
Subjective Night
MT1+/+
MT1-/-
Slo1+/+
Slo1-/-
W
N
R
ZT0
ZT6
ZT12
ZT18
ZT24
C
Subjective Day
Wake duration (min)
NREM duration (min)
REM duration (min)
***
**
+/+
-/-
Slo1
MT1
D
Subjective Night
ns

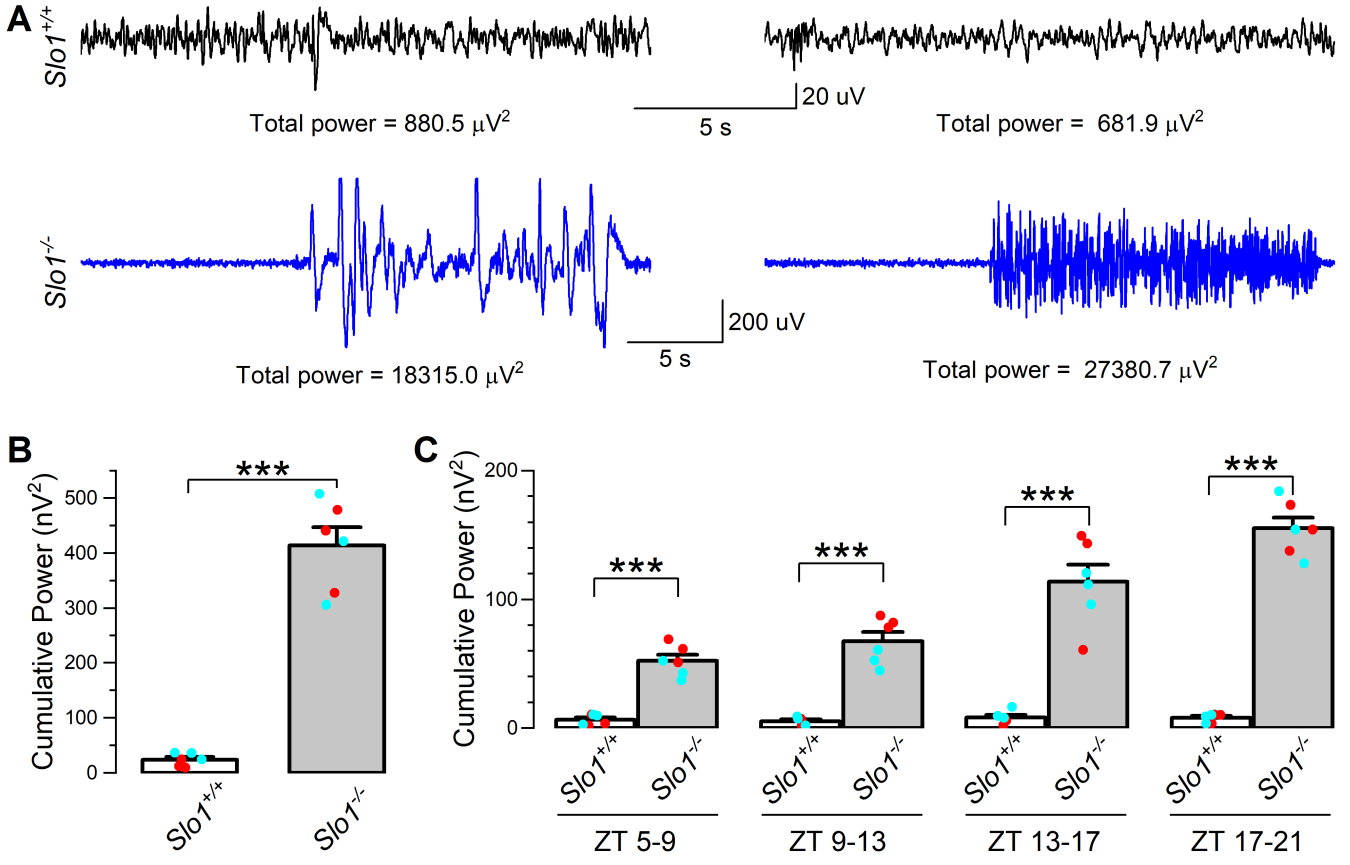
A
Slo1+/+
Total power = 880.5 μV2
20 uV
5 s
Total power = 681.9 μV2
Slo1-/-
200 uV
5 s
Total power = 18315.0 μV2
Total power = 27380.7 μV2
B
Cumulative Power (nV2)
***
Slo1+/+
Slo1-/-
C
Cumulative Power (nV2)
***
Slo1+/+
Slo1-/-
ZT 5-9
ZT 9-13
ZT 13-17
ZT 17-21

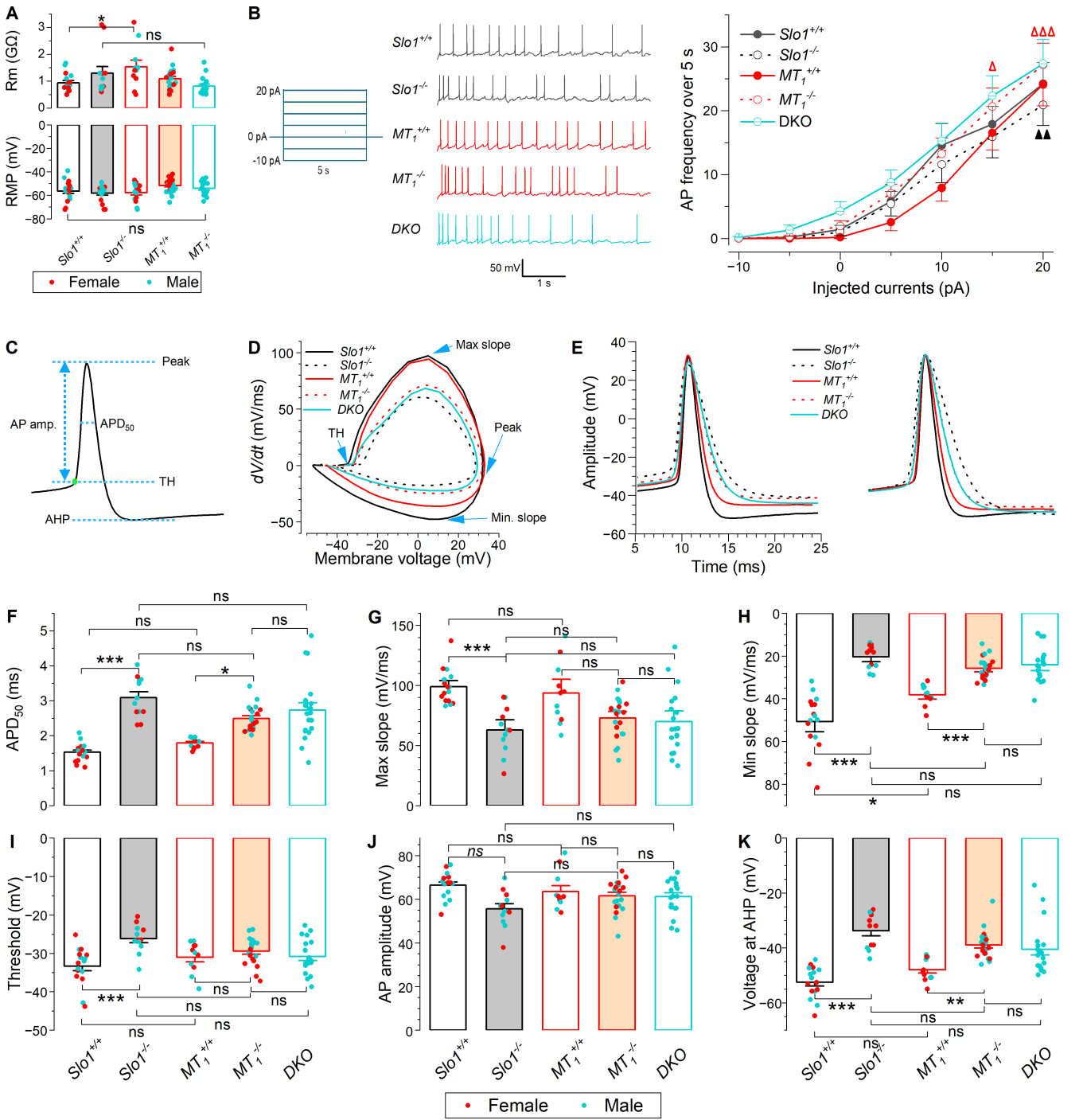
A
Rm (GΩ)
RMP (mV)
ns
Slo1+/+
Slo1-/-
MT1+/+
MT1-/-
Female
Male
B
20 pA
0 pA
-10 pA
5 s
Slo1+/+
Slo1-/-
MT1+/+
MT1-/-
DKO
50 mV
1 s
AP frequency over 5 s
Injected currents (pA)
C
Peak
AP amp.
APD50
TH
AHP
D
Max slope
Peak
TH
Min. slope
dV/dt (mV/ms)
Membrane voltage (mV)
E
Amplitude (mV)
Time (ms)
F
APD50 (ms)
G
Max slope (mV/ms)
H
Min slope (mV/ms)
I
Threshold (mV)
J
AP amplitude (mV)
K
Voltage at AHP (mV)

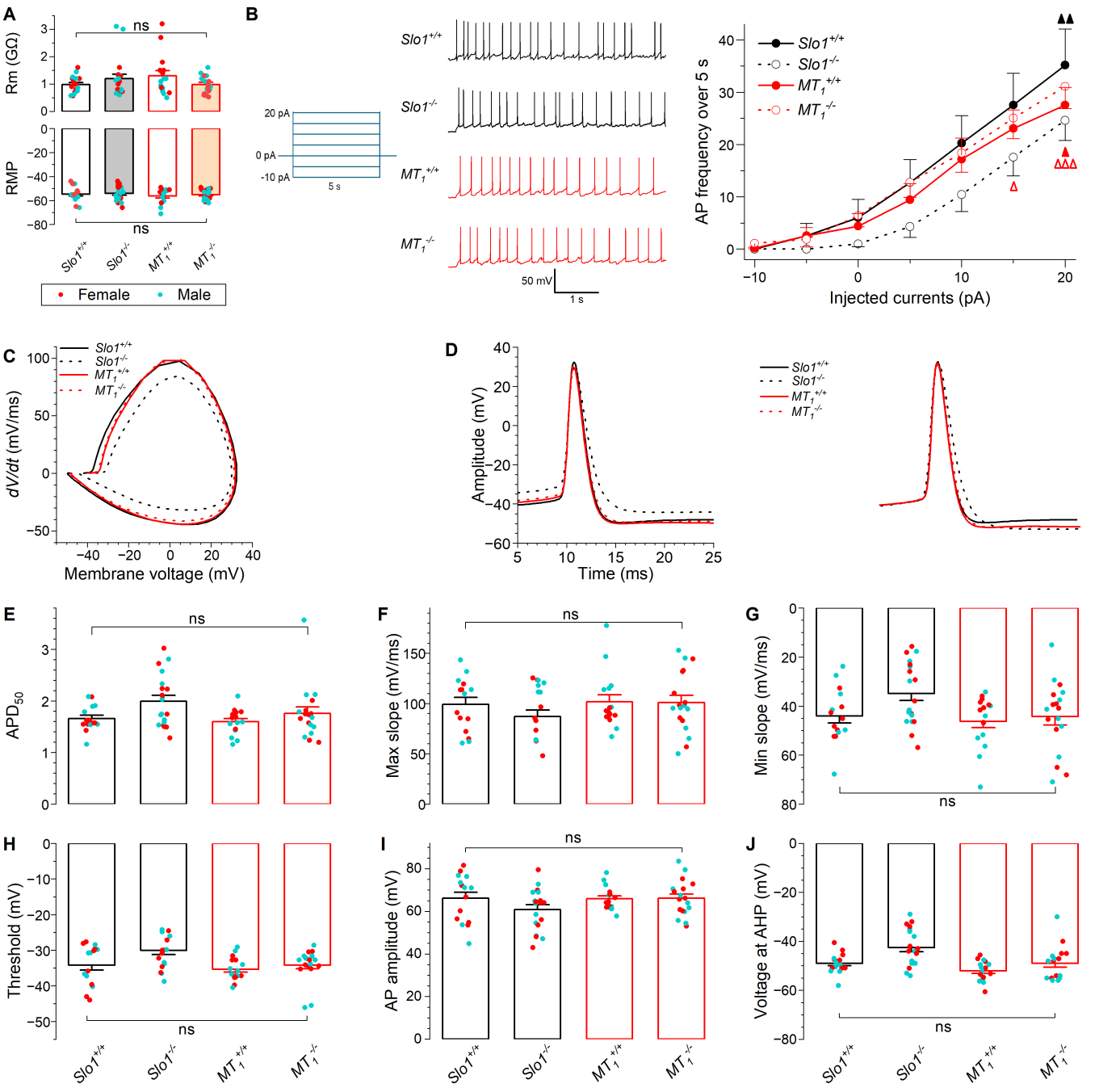
A
Rm (GΩ)
RMP
ns
ns
Slo1+/+
Slo1-/-
MT1+/+
MT1-/-
Female
Male
B
20 pA
0 pA
-10 pA
5 s
Slo1+/+
Slo1-/-
MT1+/+
MT1-/-
50 mV
1 s
AP frequency over 5 s
Injected currents (pA)
C
dV/dt (mV/ms)
Membrane voltage (mV)
D
Amplitude (mV)
Time (ms)
E
APD50
ns
F
Max slope (mV/ms)
ns
G
Min slope (mV/ms)
ns
H
Threshold (mV)
ns
I
AP amplitude (mV)
ns
J
Voltage at AHP (mV)
ns

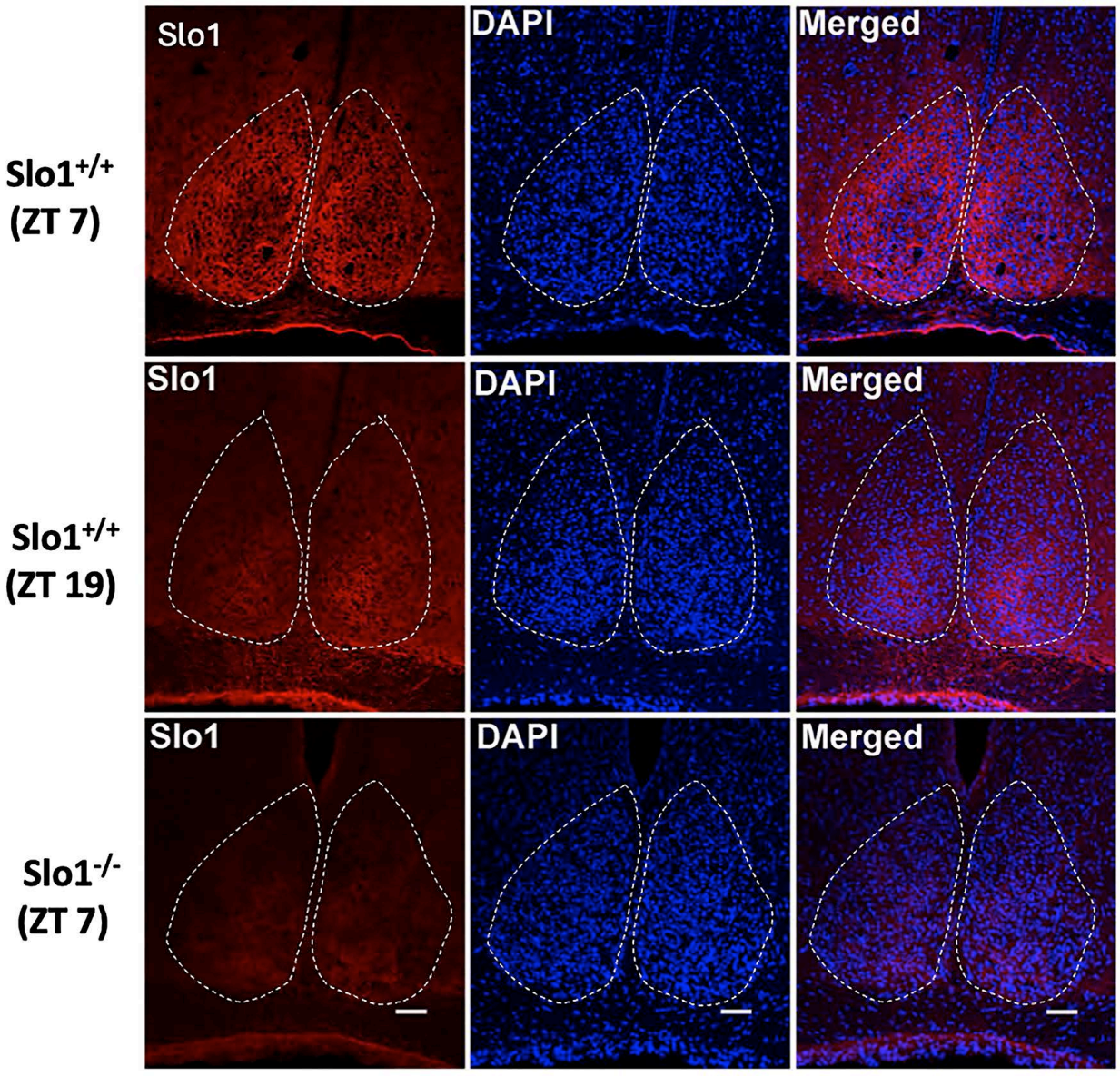
Slo1
DAPI
Merged
Slo1+/+ (ZT 7)
Slo1+/+ (ZT 19)
Slo1-/- (ZT 7)

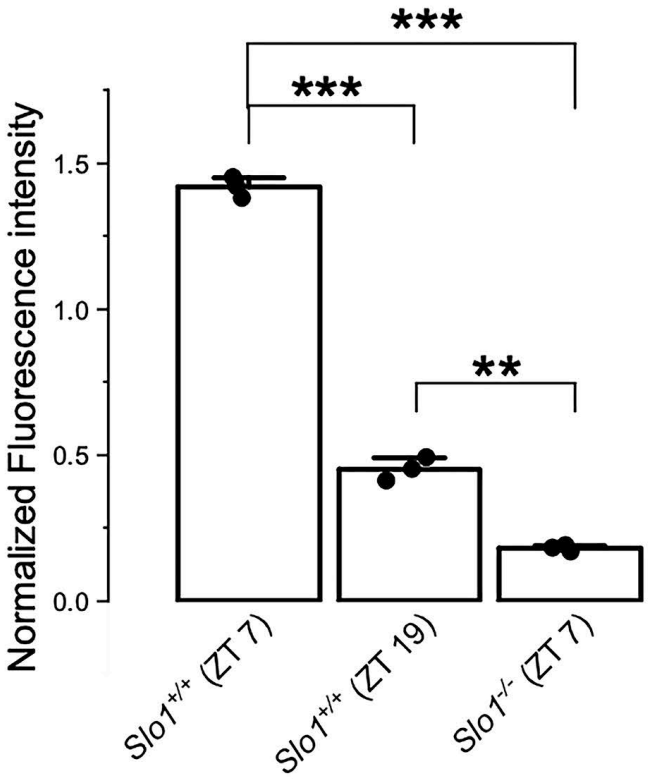
***
***
**
Normalized Fluorescence intensity
1.5
1.0
0.5
0.0
Slo1+/+ (ZT 7)
Slo1+/+ (ZT 19)
Slo1-/- (ZT 7)

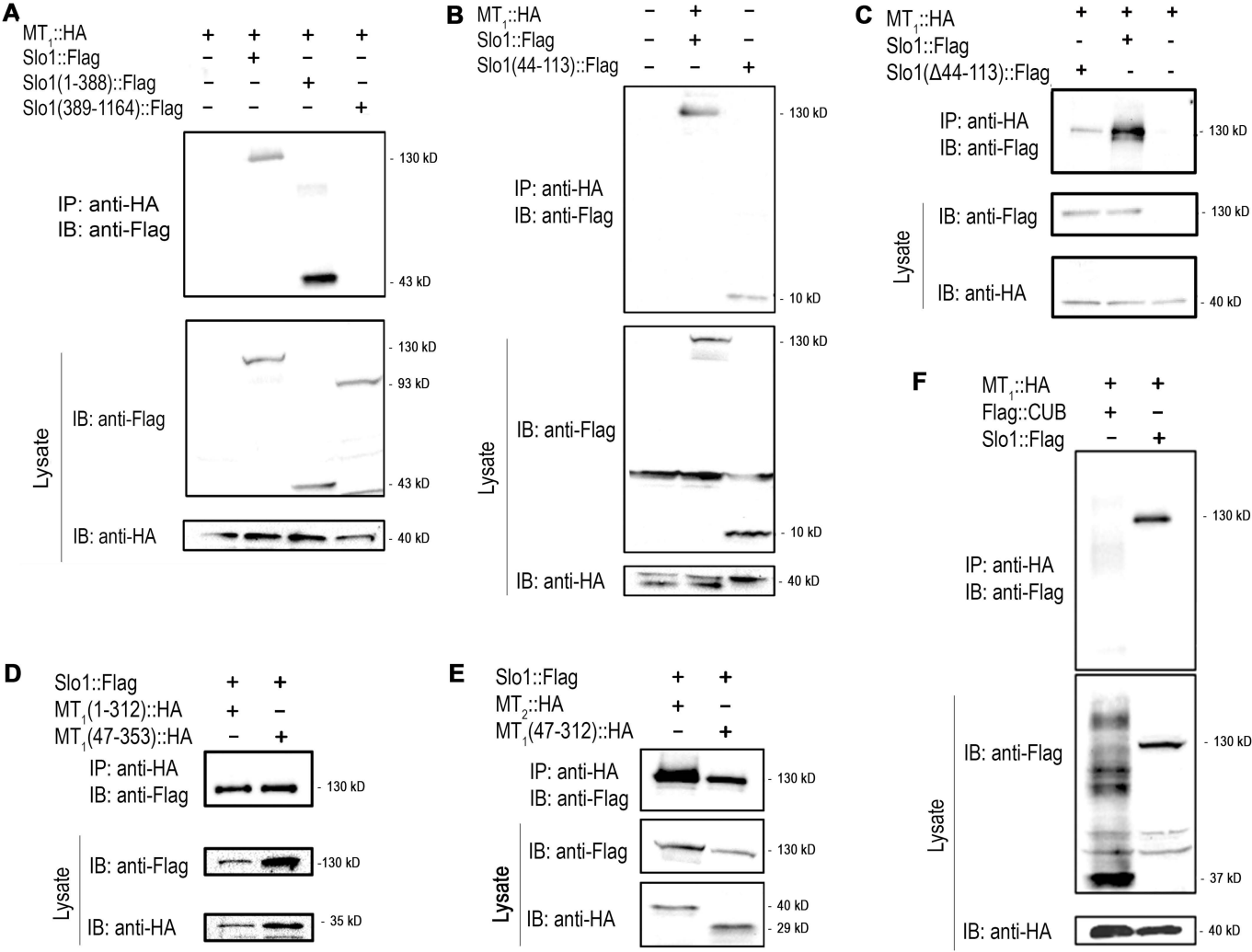
A
MT1::HA + + + +
Slo1::Flag − + − −
Slo1(1-388)::Flag − − + −
Slo1(389-1164)::Flag − − − +
IP: anti-HA
IB: anti-Flag
130 kD
43 kD
Lysate
IB: anti-Flag
130 kD
93 kD
43 kD
IB: anti-HA
40 kD
B
MT1::HA − + −
Slo1::Flag − + −
Slo1(44-113)::Flag − − +
IP: anti-HA
IB: anti-Flag
130 kD
10 kD
Lysate
IB: anti-Flag
130 kD
10 kD
IB: anti-HA
40 kD
C
MT1::HA + + +
Slo1::Flag - + -
Slo1(Δ44-113)::Flag + - -
IP: anti-HA
IB: anti-Flag
130 kD
Lysate
IB: anti-Flag
130 kD
IB: anti-HA
40 kD
D
Slo1::Flag + +
MT1(1-312)::HA + −
MT1(47-353)::HA − +
IP: anti-HA
IB: anti-Flag
130 kD
Lysate
IB: anti-Flag
130 kD
IB: anti-HA
35 kD
E
Slo1::Flag + +
MT2::HA + −
MT1(47-312)::HA − +
IP: anti-HA
IB: anti-Flag
130 kD
Lysate
IB: anti-Flag
130 kD
IB: anti-HA
40 kD
29 kD
F
MT1::HA + +
Flag::CUB + −
Slo1::Flag − +
IP: anti-HA
IB: anti-Flag
130 kD
Lysate
IB: anti-Flag
130 kD
37 kD
IB: anti-HA
40 kD

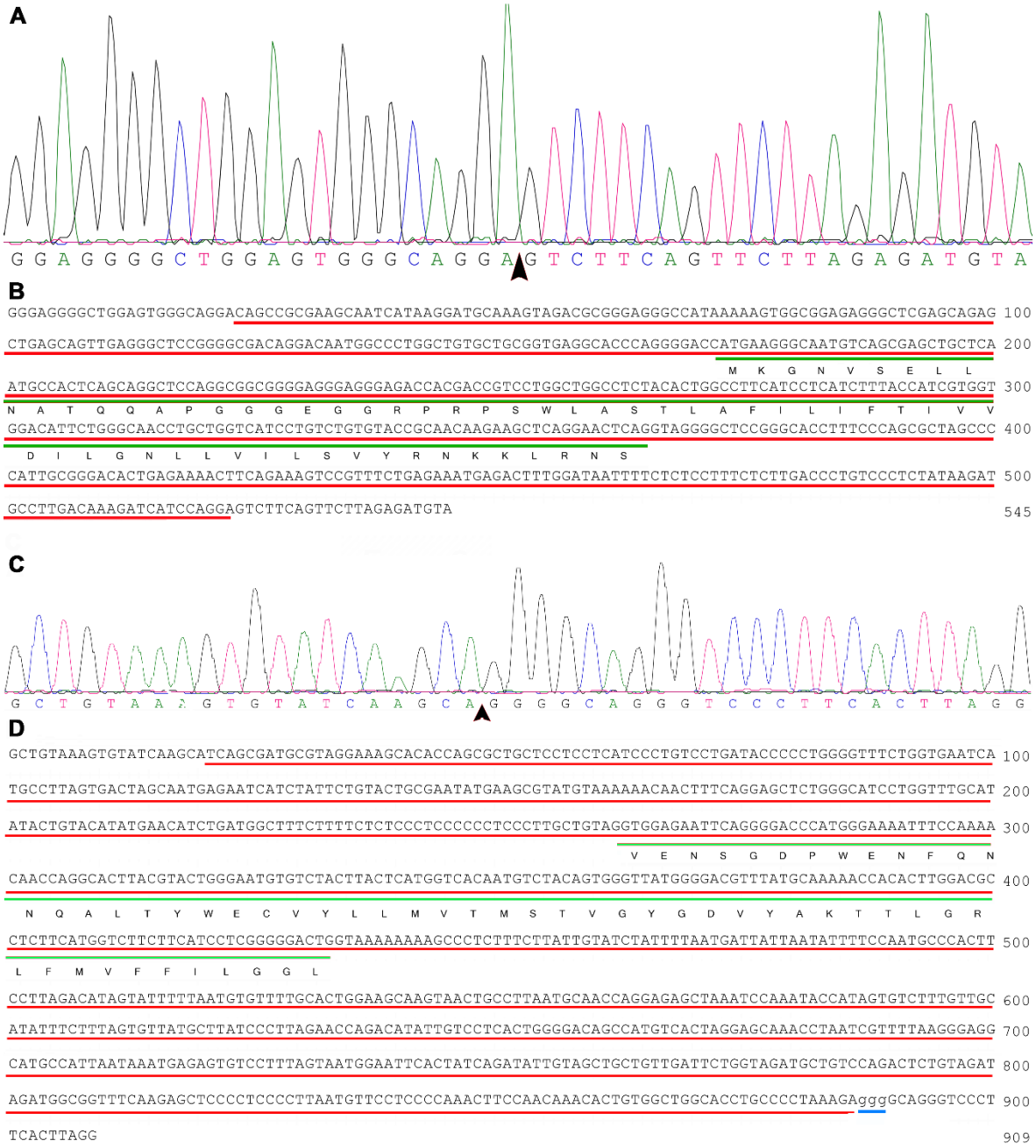

Figure S1. Deletions in *MT$_1^{-/-}$* and *Slo1$^{-/-}$* mice revealed by DNA sequencing.

(A) Chromatogram showing the location (indicated by the arrowhead) of a 500-bp deletion in the *Mtnr1a* gene.

(B) Nucleotide sequence encompassing the 500-bp deletion (underlined in red) and the flanking nucleotides matching the chromatogram. Amino acids encoded by exon 1 are underlined in green.

(C) Chromatogram showing the location (indicated by the arrowhead) of an 866-bp deletion and a 3-bp insertion in the *Kcnma1* gene.

(D) Nucleotide sequence encompassing the 866-bp deletion (underlined in red), the 3-bp insertion (underlined in blue), and the flanking nucleotides matching the chromatogram. Amino acids encoded by exon 8 are underlined in green.

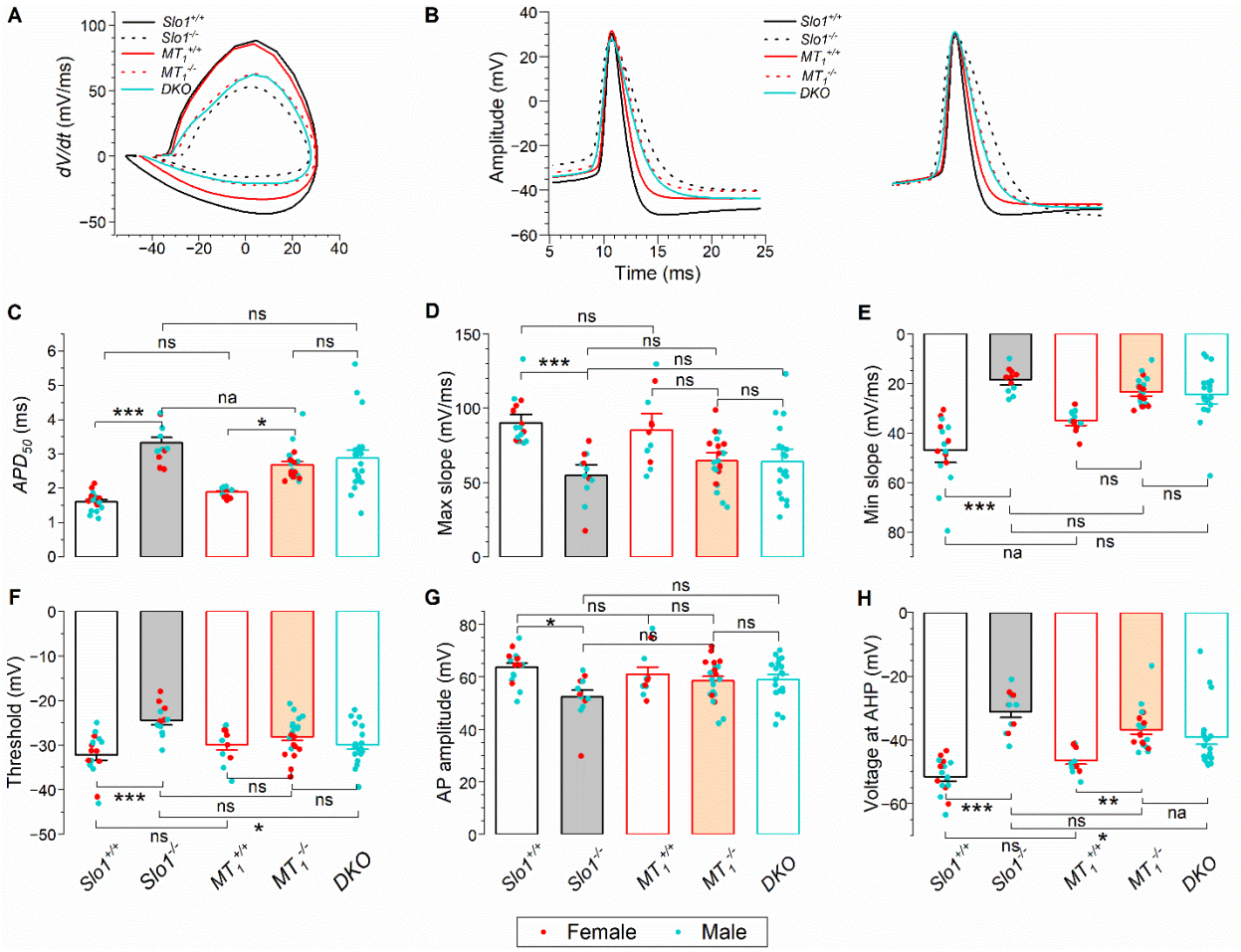

Figure S2: SCN neurons in *Slo1*$^{-/-}$ and *MT*$_1^{-/-}$ mice exhibit significant differences in APD$_{50}$ and AHP during the subjective day.

Quantitative analysis was performed on APs induced by 20 pA current injection.

(A) Voltage phase plots of averaged APs.

(B) Averaged APs, displayed as actual (left) and normalized (right) waveforms.

(C-H). Quantitative comparisons of AP-related parameters. Asterisks indicate statistically significant differences between groups (* $p < 0.05$; ** $p < 0.01$; *** $p < 0.001$), while "ns" indicates no significant difference. Statistical analyses were performed using two-way mixed-design *ANOVA* (factors: genotype and time of day) followed by Tukey's post hoc test. Blue and red dots represent data from male and female mice, respectively. Data were from the same experiments as in Figure 4.

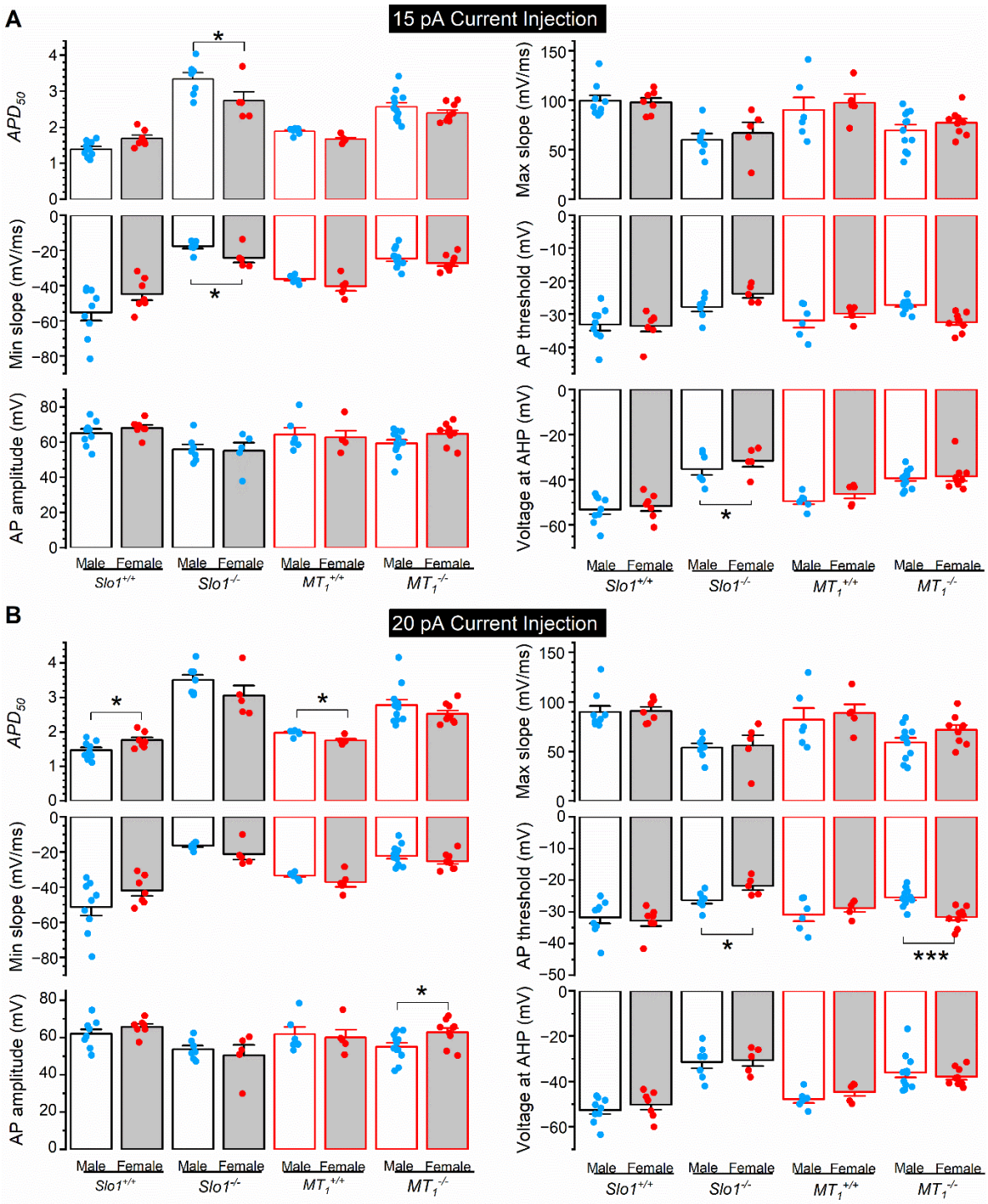

Figure S3: SCN neurons in *Slo1*$^{-/-}$ and *MT*$_1^{-/-}$ mice do not display sex-specific differences in AP-related parameters during the subjective day.

Quantitative comparisons of APs induced by 15-pA (A) and 20-pA (B) current injections between male and female mice. Statistical analyses were performed using two-way mixed-design *ANOVA* (factors: genotype and sex) followed by Tukey's post hoc test. The data are the same as those in Figure 4 and Figure S2.

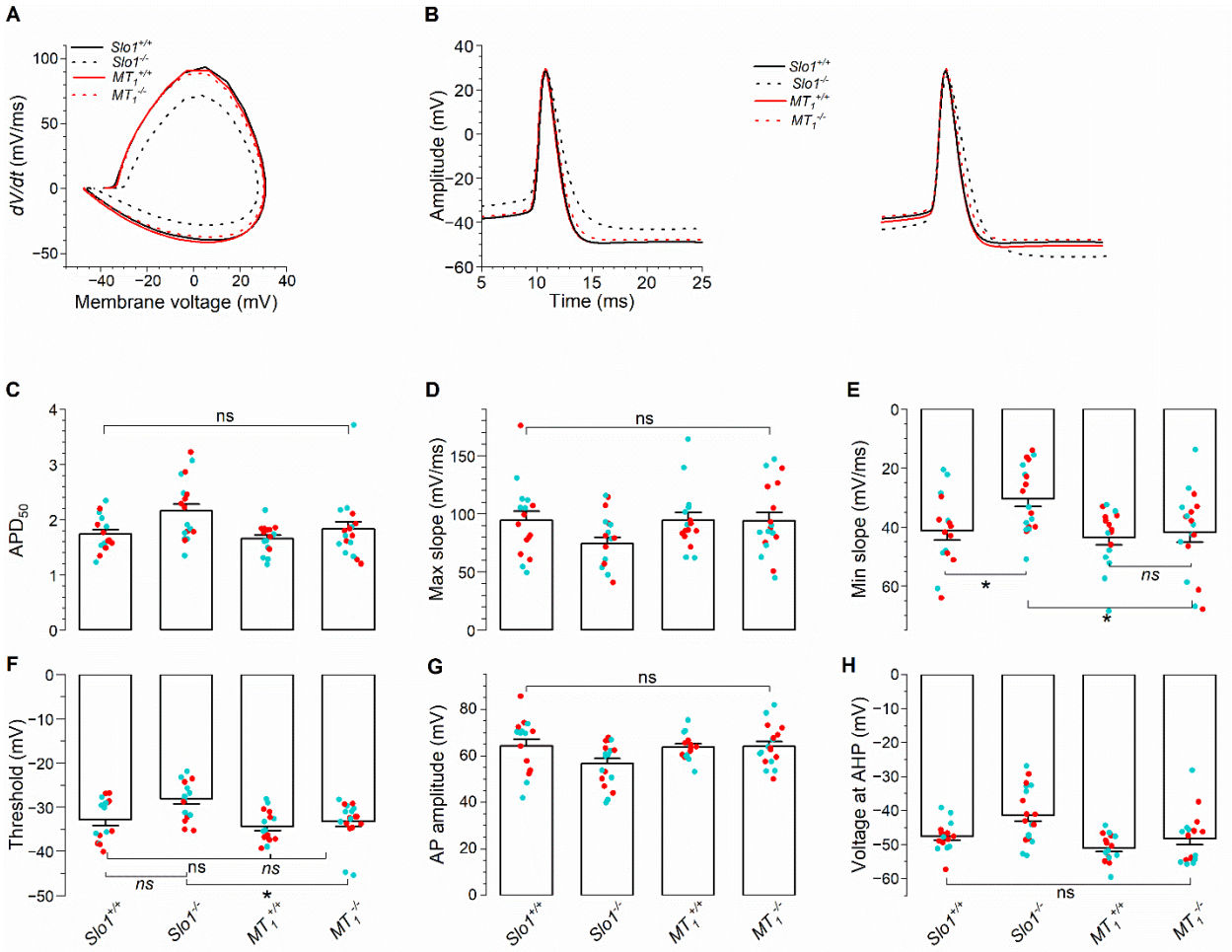

Figure S4: *Slo1*$^{-/-}$ or *MT*$_1^{-/-}$ does not alter APD$_{50}$ and AHP during the subjective night.
Quantitative analysis was performed on APs induced by 20 pA current injection.
(A) Voltage phase plots of averaged APs.
(B) Averaged APs, displayed as actual (left) and normalized (right) waveforms.
(C-H). Quantitative comparisons of AP-related parameters. Asterisks indicate statistically significant differences between groups (* $p < 0.05$; ** $p < 0.01$; *** $p < 0.001$), while "ns" indicates no significant difference. Statistical analyses were performed using two-way mixed-design *ANOVA* (factors: genotype and time of day) followed by Tukey's post hoc test. Blue and red dots represent data from male and female mice, respectively. The data are the same as those in Figure 5.

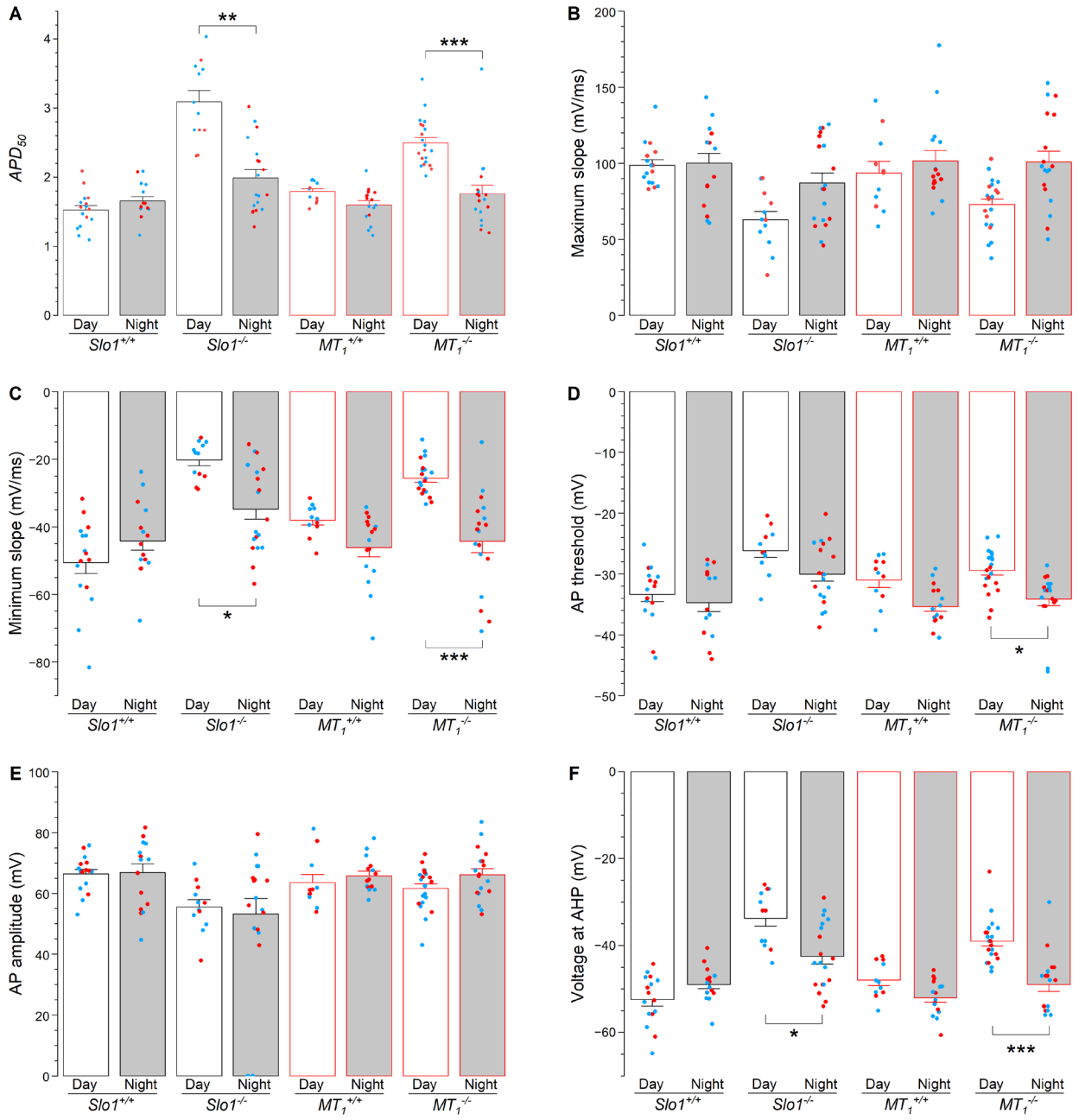

Figure S5: APD_{50} and AHP display significant differences between subjective and subjective night in *Slo1*$^{-/-}$ and *MT*$_1^{-/-}$ mice but not in their littermate controls.

(A-F) Quantitative comparisons of AP-related parameters. Asterisks indicate statistically significant differences between the indicated groups (* $p < 0.05$; ** $p < 0.01$; *** $p < 0.001$), while "ns" indicates no significant difference. Statistical analyses were performed using two-way mixed-design *ANOVA* (factors: genotype and time of day) followed by Tukey's post hoc test. The data are the same as those in Figures 4 and 5. Blue and red dots in the graphs represent data from male and female mice, respectively.